Review

For reprint orders, please contact: reprints@futuremedicine.com

Nanomedicine

Gold nanoparticles for photoacoustic imaging

Photoacoustic (PA) imaging is a biomedical imaging modality that provides functional information regarding the cellular and molecular signatures of tissue by using endogenous and exogenous contrast agents. There has been tremendous effort devoted to the development of PA imaging agents, and gold nanoparticles as exogenous contrast agents have great potential for PA imaging due to their inherent and geometrically induced optical properties. The gold-based nanoparticles that are most commonly employed for PA imaging include spheres, rods, shells, prisms, cages, stars and vesicles. This article provides an overview of the current state of research in utilizing these gold nanomaterials for PA imaging of cancer, atherosclerotic plaques, brain function and image-guided therapy.

Keywords: atherosclerosis • brain function • cancer • gold nanoparticle • photoacoustic imaging • therapy guidance

Wanwan Li[1]
& Xiaoyuan Chen*,[2]
[1]State Key Lab of Metal Matrix Composites, School of Materials Science & Engineering, Shanghai Jiao Tong University, 800 Dongchuan Road, Shanghai 200240, PR China
[2]Laboratory of Molecular Imaging & Nanomedicine (LOMIN), National Institute of Biomedical Imaging & Bioengineering (NIBIB), NIH, Bethesda, MD 20892, USA
*Author for correspondence:
Tel: +1 301 451 4246
shawn.chen@nih.gov

Photoacoustic (PA) imaging is a rapidly emerging biomedical imaging modality based on the PA effect that was first observed by Alexander G Bell in 1880 [1]. Through PA imaging, it is possible to obtain information in real time with a high spatial resolution on the anatomical, functional and molecular content of diseased tissues in the absence of ionizing radiation [2–6]. Compared with fluorescence optical imaging, PA imaging has higher spatial resolution (as low as 5 μm) and a deeper imaging depth (up to 5–6 cm) due to the much weaker scattering of ultrasonic signals than light in tissue. Compared with ultrasound imaging, whose contrast is limited by the mechanical properties of biological tissues, PA imaging has better tissue contrast, which is related to the optical properties of different tissues. Moreover, the absence of ionizing radiation also makes PA imaging safer than computed tomography and the radionuclide-based imaging techniques of PET and SPECT. Endogenous contrast can be used in PA imaging to provide functional and even anatomical information. In particular, these imaging modes can be greatly enhanced by exogenous contrast agents and allow for imaging of cellular and molecular events. Currently, a great variety of PA contrast agents exists, and gold nanoparticles (AuNPs) are one of the most promising exogenous PA contrast agents.

Due to their strong and tunable optical absorption that results from the surface plasmon resonance (SPR) effect, AuNPs have been widely used as PA contrast agents in recent years. The SPR effect occurs when free charges on the surface of AuNPs oscillate with the electromagnetic field, leading to an optical absorption that is several orders of magnitude greater than organic dyes [7]. When the size and shape of the AuNP change, its resonant frequency also changes, which enables researchers to exploit the use of the wavelength range of the ‘biological window’ (650–1100 nm), in which the least blood and tissue attenuation occurs. Therefore, a high visible contrast can be obtained with particles absorbing in the ‘biological window’ [8], which is very important for the PA imaging of targeted areas located deep within biological tissues that cannot be realized by other superficial methods [9]. Moreover, there also exists the second near-infrared (NIR) spectral window (1100–1350 nm) of minimal water absorption between water peak maxima [10,11]. At longer NIR wavelengths in this region, scattering is reduced due to the inverse wavelength dependence from Rayleigh scattering and due to Mie scattering at longer wavelengths. Thus, contrast agents absorbing in the second NIR spectral window also show their potential in PA imaging. Currently, the research on AuNPs has made it possible to precisely control their synthesis in terms of size, shape and uniformity. Besides the original colloidal gold nanospheres (AuNSs) [12], many research groups have developed more complicated nanostructures, such as gold nanorods (AuNRs) [13], gold nanoshells (AuNShs) [14], gold nanoprisms (AuNPrs) [15], gold nanocages (AuNCs) [16], gold nanostars (AuNSts) [17], gold nanovesicles [18] and rhombic dodecahedra and bipyramids (Figure 1) [19].

Therefore, this article aims to overview the current research that has incorporated the use of AuNPs in PA imaging both *in vitro* and *in vivo*. AuNPs have been functionalized with different surface modifiers in order to further enhance the imaging contrast; however, this article will limit its scope to PA imaging that mainly utilizes the optical properties of AuNPs themselves. First, the optical properties of AuNSs, AuNRs, AuNShs, AuNPrs, AuNCs, AuNSts and gold vesicles are described. Then, the role of these nanostructures in the field of PA imaging of cancer, atherosclerotic plaques, brain function and PA imaging-based therapy guidance are discussed.

PA imaging basics

PA imaging capitalizes on the PA effect, which is simply the generation of an acoustic wave resulting from the absorption of optical energy. Briefly, laser energy absorbed by endogenous chromophores or exogenous contrast agents causes a rapid thermoelastic expansion of tissue, resulting in the generation of a wide-band ultrasound wave originated from the photoabsorber. The ultrasound wave can be detected with a transducer that converts the mechanical acoustic waves to electric signals, which are then processed to form an image [5,20–21]. A typical PA imaging setup consists of two main components: a tunable nanosecond pulsed laser and a user–system interaction system (Figure 2).

The maximum initial pressure (P_0) generated after thermoacoustic excitation in the photoabsorber is described in Equation 1, assuming 1D plane wave propagation in a homogeneous medium:

$$P_0 = \frac{\beta \nu_s^2}{c_p} \mu_a F_0 e^{-\mu_{eff} z} = \Gamma \mu_a F_0 e^{-\mu_{eff} z}$$

where β represents the thermal coefficient of volume expansion, v_s represents the speed of sound in tissue, C_p represents the specific heat capacity of the tissue at a constant pressure, μ_a is the optical absorption coefficient of the photoabsorber, F_0 is the laser fluence at depth $z = 0$, Γ is the Grüneisen parameter of the tissue and μ_{eff} represents the effective extinction coefficient of the tissue, which can be defined in Equation 2 as:

$$\mu_{eff} = \sqrt{3\mu_a\left(\mu_a + \mu_s'\right)}$$

where μ_s' is the reduced scattering coefficient of tissue [5,20–22].

The spatial resolution in PA imaging is determined by the characteristics of an ultrasound transducer [2,20,23]. As for deep-penetrating PA imaging, the axial resolution is inversely proportional to the bandwidth (BW) of the transducer, and the lateral resolution is inversely proportional to both the numerical aperture and center frequency of the transducer. Therefore, a transducer with a high BW, large numerical aperture and high center frequency yields high-resolution images [2,20].

Laser light penetration and acoustic attenuation in the tissue limits the penetration depth in PA imaging. The penetration depth is primarily limited by the optical scattering and determined by the effective extinction coefficient μ_{eff}. At depths greater than 1 mm, the laser light diffuses and decays exponentially with the exponential constant equal to μ_{eff}, and penetration depth is strongly wavelength dependent and may reach up to several centimeters in the biological window (650–1100 nm). Depths of up to 5–6 cm have been reported [24–26] by using radiant exposures below the maximum permissible exposure, which is imposed by the American National Standards Institute for human skin (the maximum permissible exposure limit at different wavelengths is 20 mJ/cm^2 at $400 < \lambda < 700$ nm, $20 \times 10^{0.002(\lambda - 700)}$ mJ/cm^2 at $700 < \lambda < 1050$ nm and 100 mJ/cm^2 at $1050 < \lambda < 1500$ nm [27]).

There is a trade-off between resolution and imaging depth of PA imaging. When the imaging depth increases, frequency-dependent attenuation decreases the center frequency and BW of the ultrasound wave, resulting in lower spatial resolution [20]. Therefore, a PA microscopy system sacrifices imaging depth to improve resolution of 50 μm [20,28–30], and a lateral resolution as low as 5 μm can be reached for imaging superficial capillaries by using a highly focused laser beam [29]. Conversely, macroscopic PA imaging systems are promising for tumor detection in deeper regions with a resolution on the order of hundreds of microns [24–26,31].

The contrast in PA imaging is largely determined by the wavelength-dependent optical absorption coef-

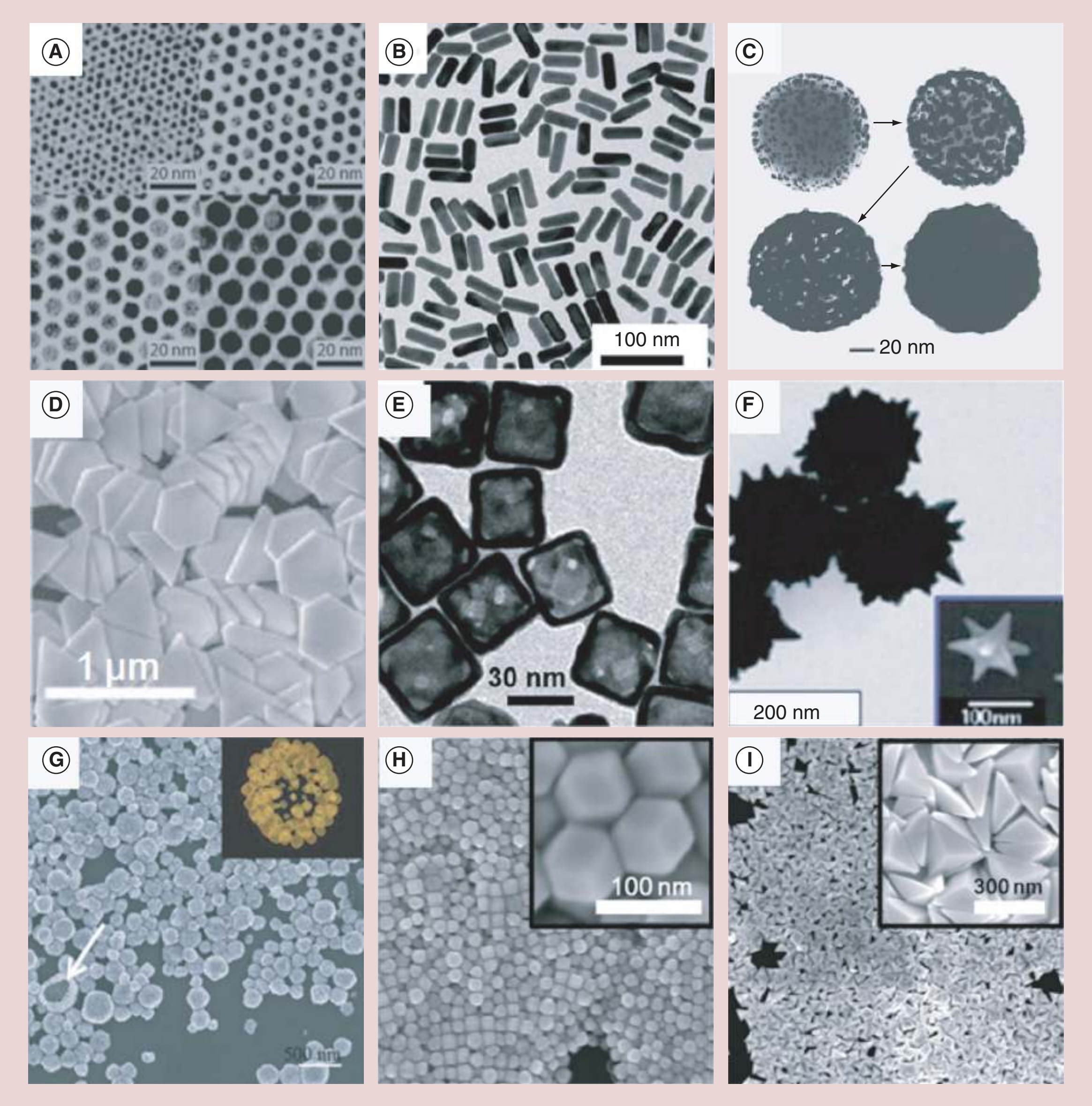

Figure 1. Scanning electron microscope and transmission electron microscope micrographs of gold nanostructures of various shapes and sizes. **(A)** Nanospheres, **(B)** nanorods, **(C)** nanoshells, **(D)** nanoprismss, **(E)** nanocages, **(F)** nanostars, **(G)** nanovesicles, **(H)** rhombic dodecahedras, and **(I)** bipyramids..

ficient μ_a. Due to the large variations of endogenous chromophores (melanin, oxy-[HbO_2] and deoxyhemoglobin [Hb]) in μ_a, spectroscopic or multiwavelength imaging techniques can be used to characterize the optical properties of tumor tissue. Thus, different wavelength-dependent optical absorption properties of HbO_2 and Hb enable spectroscopic PA imaging in order to differentiate between arteries and veins. Due to the same optical absorption of HbO_2 and Hb at approximately 805 nm, PA imaging at this and other wavelengths can be utilized in order to assess total hemoglobin and blood oxygenation. Moreover, PA contrast can be enhanced by exogenous contrast agents that have distinct and tunable absorption spectra in the biological window.

Plasmonic AuNPs

When AuNPs interact with light, the SPR effect occurs when the conduction electrons of the metal are driven by the incident electric field into collective oscillations known as localized SPRs (LSPRs) [32,33]. The local field intensities of electromagnetic fields on the nanostructure surface resulting from LSPRs can be orders of magnitude greater than those of the incident field. The electromagnetic fields can enhance both the radiative and nonradiative properties of AuNPs, thus

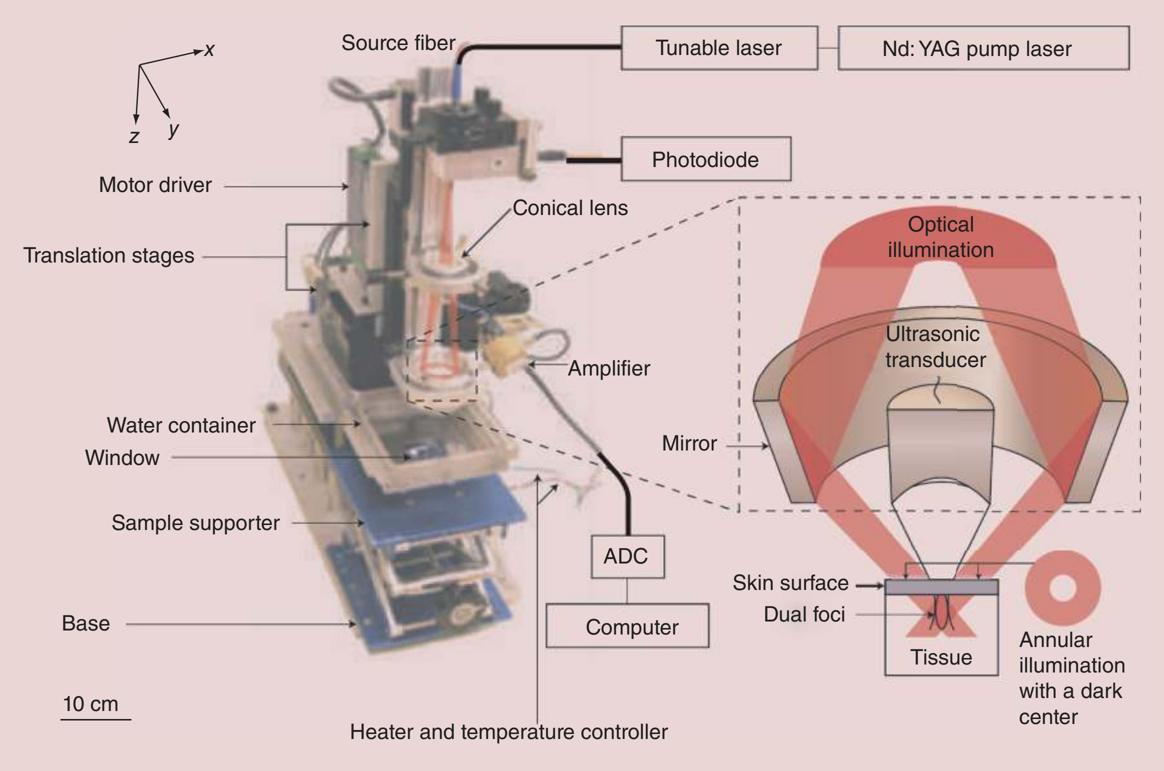

Figure 2. Dark-field confocal photoacoustic microscope.
ADC: Analog-to-digital converter; Nd:YAG: Neodymium-doped yttrium aluminum garnet.

directly impacting biomedical imaging and therapy. Following illumination, plasmons can either decay nonradiatively or radiatively, resulting in absorption or light scattering, respectively. Thus, the strong extinction peaks (LSPR) of AuNPs in the visible and NIR regions are usually composed of two components of absorption and scattering. By changing the size, shape and internal structure of the AuNPs, the relative magnitude of light being absorbed and scattered can be tuned, and optical absorbing-dominant AuNPs are more valuable for PA imaging. Therefore, it is essential to know both the absorption cross-section (σ_a) and the scattering cross-section (σ_s) of a nanostructure for a specific biomedical application. A technique [34] has been developed that combines the well-known Beer–Lambert law with PA imaging in order to measure σ_a, together with the overall extinction cross-section (σ_e) obtained using a ultraviolet–visible–NIR spectrometer, then the σ_s and the contributions of σ_a and σ_s to the optical properties of the gold nanostructures can be calculated, which can be well controlled by modulating the dimensions for AuNRs and AuNCs [35]. Due to the low absorption of NIR light by biological fluids and greater photon penetration depth attained by NIR light with minimal tissue damage, AuNPs resonant in this region enable deep tissue PA imaging and therapy guidance.

Typical plasmonic AuNPs

Plasmonic AuNPs have been synthesized in a myriad of shapes and sizes, each of which possesses unique optical characteristics. AuNP synthesis methods vary greatly among different types of particles, and there are also many routes to obtaining similar shapes. A detailed discussion of different synthesis techniques is beyond the scope of this article, but they are readily available in other articles [36,37]. The following are some typical AuNPs with distinct and tunable absorption spectra suitable for PA imaging (Figure 3).

AuNSs are the most basic shapes that can be synthesized. It is well known that AuNSs produce a single absorption, typically at approximately 520 nm [7], which can be tuned to a maximum of approximately 600 nm when the particle size goes up to 100 nm [38]. This is the major disadvantage for the use of AuNSs in PA imaging, as contrast is greatly decreased outside of the biological window [39]. The optical absorption spectrum near 520 nm is similar to that of blood, which makes it difficult to distinguish individual particles from blood *in vivo*. However, the hierarchical assembly of AuNSs allows one to engineer the LSPR peaks to the NIR region owing to a strong plasmonic coupling effect between adjacent AuNSs [40]. For the vesicular/clustered gold vesicle assemblies composed of polyethylene oxide-*b*-polystyrene-tethered AuNSs, the LSPR peaks can be tuned in the range of 650–800 nm [41,42]. For the biodegradable gold vesicles composed of PEG-*b*-poly(ε-caprolactone)-tethered AuNSs, the LSPR peaks were broadened, and the major peak moved to approximately 1000 nm as the AuNS concentration increased [43].

AuNRs are extensively applied in PA imaging because of their facile synthesis route and tunable absorption in the NIR region [44,45]. The cylindrical conformation of AuNRs shows a unique optical effect due to the presence of two critical dimensions of the long axis and the short axis, and the aspect ratio (length:width) is commonly used to identify nanorod sizes [46]. The oscillation of the long axes (known as the longitudinal band) contributes to characteristic specific absorbance wavelengths, while the transverse absorption band is sustained at approximately 520 nm, which is relatively unaffected by nanorod size [38,47]. When the aspect ratio increases, the absorbance of the longitudinal band shifts deeper into the NIR region, and absorption peaks as high as 1300 nm have been attained [44]. However, AuNRs with aspect ratios of between 3 and 4 were found to be optimal for PA imaging, as their absorption falls within the biological window [48–51]. The optical absorbance and scattering cross-sections of AuNRs are a function of size, thus larger AuNRs produce increased scattering and smaller AuNRs produce increased absorbance. Moreover, small AuNRs with high aspect ratios are expected to absorb light, while larger AuNRs with lower aspect ratios can scatter light more prominently [7].

AuNShs have also been used as PA imaging contrast agents [52,53]. The initial AuNShs used a core–shell system with an inner Au_2S core [54], which were improved to silica cores covered with gold [14,55–56]. Studies on determining the optical tunability of these systems indicated that thinner shells over larger cores can increase the resonance shift from ultraviolet–visible spectroscopy to between 800 and 2200 nm [57,58]. In addition, another class of AuNShs with a hollow inside have also been investigated. In 2002, the Xia group developed a new template replacement method to synthesize hollow metal nanostructures, which significantly improved the ability to form shell walls with uniformity and face centered cubic crystallinity [59]. However, AuNShs exhibit more scattering than absorption and a broad optical spectrum, which makes them less effective PA contrast agents than AuNRs [60].

AuNPrs also show promise for PA imaging at longer wavelengths [61]. One of the first observations of spectroscopically identifiable AuNPrs from a thermal synthesis was made by Malikova *et al.* [62]. The resulting NP solution contained a mixture of plate-like nanostructures and pseudospherical NPs, and the extinction spectrum from this mixture showed two distinct bands corresponding to the SPRs from the two types of particles. The Mirkin group used a seed-mediated, surfactant-based system that produced a mixture of AuNPrs and pseudospherical NPs, each with relatively narrow size distributions (nanoprism edge length: 144 ± 30 nm; NP diameter: 35 ± 2 nm) [15,63]. The synthetic method was subsequently used to control the edge length of AuNPrs at between 100 and 300 nm by using the nanoprisms themselves as seeds [64]. Higher-order plasmon modes have also been observed from prisms produced from a synthesis described by Ah *et al.*, wherein poly(vinylpyrrolidinone) was used as a capping ligand and shape-directing moiety [15]. The resulting AuNPrs were single crystals with planar widths of 80–500 nm and thicknesses of 10–40 nm, exhibiting strong surface plasmon absorption in the region of 700–2000 nm.

AuNCs have been developed because they show similar optical characteristics to AuNShs, but with much smaller sizes [39,65–66]. Recently, research has been carried out in order to synthesize double-shelled AuNCs by using different combinations of gold, platinum and palladium layers [67]. In addition to the adjustment of the amount of $HAuCl_4$ used, the size of the silver nanocube template can fine tune the SPR properties of the AuNCs. More explicitly, SPR of AuNShs can be affected by variations in cage size, wall thickness and number of truncated corners [68]. The advantages of these AuNShs are their reproducibility, their compact nature (NIR absorbance is achieved at small sizes [35–40-nm nanocages for 800-nm peak absorbance]), their LSPR peaks (which can be easily and precisely tuned in the range of 600–1200 nm), their sizes (which can be readily varied from 20 to 500 nm with greatly enhanced absorbance cross-sections over conventional dyes) [68] and their encapsulation abilities [69].

AuNSts are spiked AuNSs that can also be used in PA imaging [17,70]. There are two general approaches to synthesizing AuNSts [71]. The unusual optical properties of AuNSts make them ideal candidates for many biomedical NIR absorption applications, including PA imaging. The branching and sharp tips result in a dominating second resonance presence in addition to the resonance produced by the core of the particle [72]. The peak resonance of AuNSts increases with the increase of the number, the length and the tip sharpness of the branches, and the second plasmon of AuNSts can be tuned into the range of 650–900 nm, while the overall AuNSt size is relatively irrelevant [72–74]. Due to the larger reactive surface area, biocompatibility and feasible optical tunability, AuNSts have encouraged researchers to take advantage of these properties in PA imaging [75].

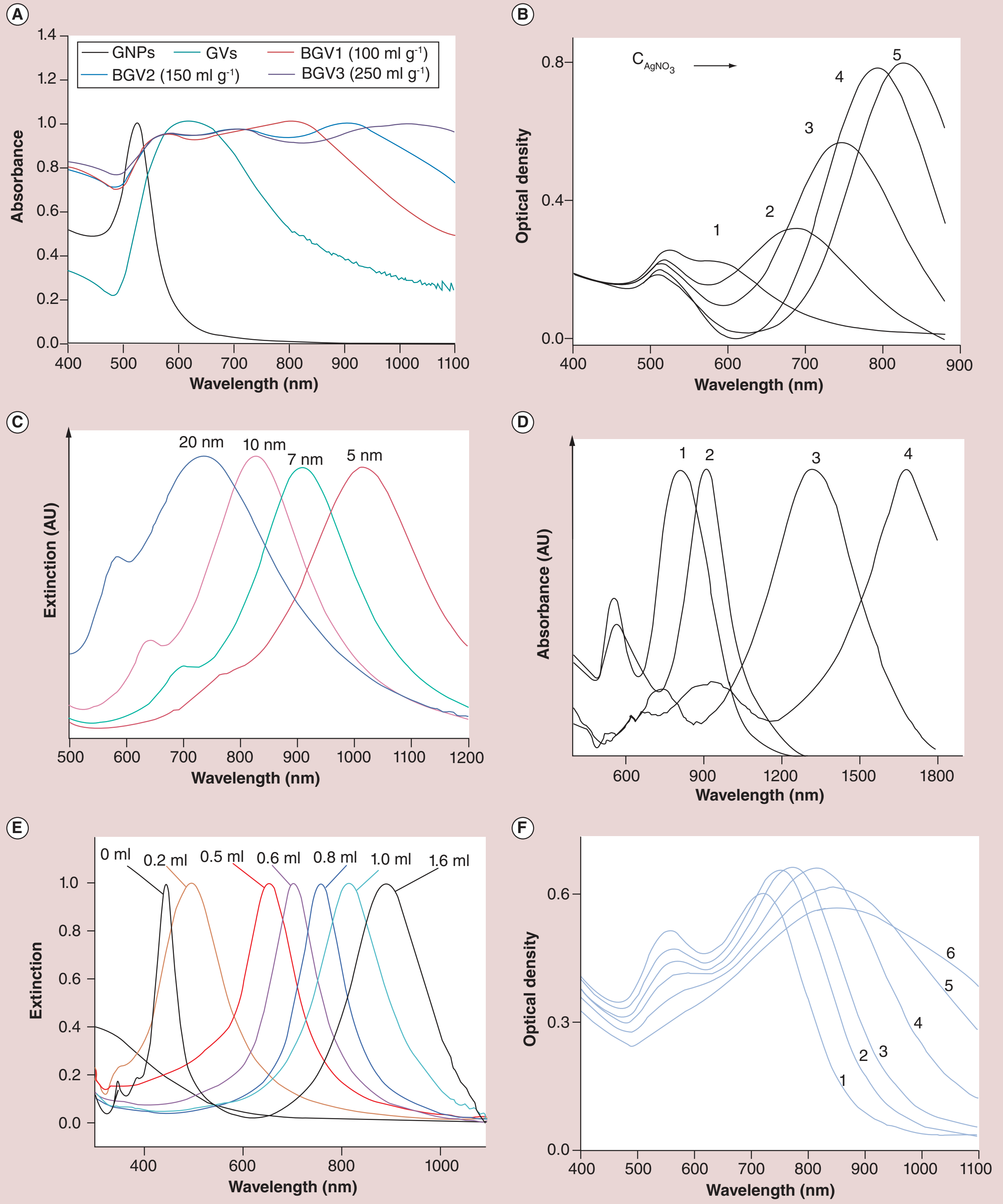
A
Absorbance
1.4
1.2
1.0
0.8
0.6
0.4
0.2
0.0
GNPs
GVs
BGV1 (100 ml g^{-1})
BGV2 (150 ml g^{-1})
BGV3 (250 ml g^{-1})
400 500 600 700 800 900 1000 1100
Wavelength (nm)
B
Optical density
0.8
0.4
0.0
C_{AgNO_3}
1
2
3
4
5
400 500 600 700 800 900
Wavelength (nm)
C
Extinction (AU)
20 nm
10 nm
7 nm
5 nm
500 600 700 800 900 1000 1100 1200
Wavelength (nm)
D
Absorbance (AU)
1
2
3
4
600 900 1200 1500 1800
Wavelength (nm)
E
Extinction
1.0
0.8
0.6
0.4
0.2
0.0
0 ml
0.2 ml
0.5 ml
0.6 ml
0.8 ml
1.0 ml
1.6 ml
400 600 800 1000
Wavelength (nm)
F
Optical density
0.6
0.3
0.0
1
2
3
4
5
6
400 500 600 700 800 900 1000 1100
Wavelength (nm)

Figure 3. Tunability of plasmon resonances of different gold nanoparticles (see facing page). (A) UV-Vis-NIR spectra of AuNSs, PEG-b-PS-tethered gold vesicles, and block-copolymer-tethered biodegradable gold vesicles produced by the dialysis of solutions of AuNSs (100, 150, and 250 mg/ml) in THF. The LSPR of the biodegradable gold vesicle can be tuned by varying the AuNS concentration. **(B)** UV–visible–NIR absorption spectra of AuNRs synthesized with different amounts of $AgNO_3$ solution (0.0040 M) of 0.050 ml (1), 0.10 ml (2), 0.15 ml (3), 0.20 ml (4), 0.25 ml (5). The LSPR peak could be precisely tuned by varying the concentrations of $AgNO_3$ in the growth solution (aspect ratios of AuNRs). **(C)** Normalized UV–visible–NIR extinction spectra of gold shell-silica core AuNShs as a function of their core/shell ratio (60 nm core radius/different shell thickness). **(D)** UV-vis-NIR absorption spectra of the gold nanoprisms with average width and thickness of 450 ± 29 and 39 ± 4 nm (1), 310 ± 25 and 28 ± 3 nm (2), 158 ± 13 and 18 ± 3 nm (3), and 96 ± 12 and 14 ± 2 nm (4). Values given as mean ± standard deviation. **(E)** UV-vis-spectra of the AuNCs obtained by titrating the Ag nanocubes with different amounts of aqueous $HAuCl_4$ solution. The LSPR of the Au nanocages is tunable by varying the volume of $HAuCl_4$ solution added. **(F)** Absorption spectra of AuNSts with average core size and branch length of 27 ± 2 and 12 ± 2 (1), 27 ± 2 and 13 ± 3 (2), 31 ± 3 and 15 ± 3 (3), 39 ± 3 and 19 ± 4 (4), 46 ± 4 and 22 ± 5 (5), 57 ± 5 and 28 ± 7 (6). Values given as mean ± standard deviation.

AU: Arbitrary unit; AuNC: Gold nanocage; AuNR: Gold nanorod; AuNS: Gold nanosphere; AuNSh: Gold nanoshell; AuNSt: Gold nanostar; BGV: Biodegradable gold nanovesicle; C_{AgNO_3}: $AgNO_3$ concentration; GNP: Gold nanoparticle; GV: Gold vesicle; LSPR: Localized surface plasmon resonance peak; NIR: Near-infrared.

For color figures, see online at www.futuremedicine.com/doi/full/10.2217/NNM.14.169.

Comparison of plasmonic AuNPs with other PA contrast agents

In addition to the plasmonic AuNPs, there are many other PA contrast agents, including the NIR-absorbing dyes (indocyanine green) [76], methylene blue [77], IRDye® 800CW (Li-Cor Biosciences, NE, USA) [78], Alexa Fluor® (Life Technologies, CA, USA) 750 [79]), single-walled carbon nanotubes (SWNTs) [80], plasmonic silver nanoparticles (NPs) [81] and hybrid contrast agents [82–85], as shown in Table 1.

The NIR-absorbing dyes are typically small molecules with sizes in the order of 1 nm, which can be quickly cleared from the body through the renal system and therefore do not provide sufficient time for them to label their molecular targets. They also suffer from photobleaching and can permanently degrade in several minutes under normal PA imaging conditions [93]. Moreover, compared with AuNPs, these dyes have an absorbance that is orders of magnitude lower than that of AuNPs.

Nonplasmonic NPs of SWNTs absorb over a broad spectrum, including the optical window, resulting in a large PA signal [80]. However, the broad absorption spectra without distinct peaks limit their application in SPR peak wavelength-dependent PA imaging. Plasmonic silver NPs with tunable SPR peaks have been introduced as PA contrast agents [81]; however, the tunability of the SPR peaks by sizes and shapes is much weaker than that of AuNPs.

Moreover, some PA imaging-based hybrid contrast agents were developed in order to act as contrast agents in two or more imaging modalities. These hybrid contrast agents can provide further detailed molecular information with an enhanced contrast (indocyanine green-enhanced SWNTs [82]) or can be used to provide contrast for multiple imaging modalities (gold-coated SWNTs [83], iron oxide–AuNShs [84] or magnetic NPs [MNPs] and gold-coated SWNTs [85]).

AuNP-based PA diagnostic imaging

Cancer imaging

Primary tumor imaging

AuNP-based PA imaging is well suited to detecting various types of tumors because these plasmonic AuNPs can be accumulated in tumors through the enhanced permeability and retention effect or be functionalized in order to accumulate through receptor-mediated binding, which can be used to indicate the presence of a tumor.

It was reported that AuNSs could be utilized to detect human breast cancer tumor xenografts at a wavelength of 532 nm [94]. AuNCs were also utilized in PA imaging in order to detect B16 melanomas at 778 nm (Figure 4A–C) [95] and U87 brain tumors [96]. It was also reported that the passive accumulation of silica-coated AuNRs in a xenografted tumor can be monitored through spectroscopic PA imaging, which is capable of visualizing the presence of exogenous contrast agents *in vivo* through obtaining PA signals at multiple wavelengths and finding a map of different optical absorbers (Figure 4D–G) [97,98].

The feasibility of using AuNRs with different absorption spectra and multiplex targeting moieties to image multiple types of cancer has been demonstrated both *ex vivo* [99,100] and in a mouse model [101]. PEGylated AuNPrs were also successfully used as signal amplifiers in multispectral optoacoustic tomography to visualize gastrointestinal cancer. In order to specifically target overexpressed integrin $\alpha_v\beta_3$ on the tumor neovasculature, cyclic Arg–Gly–Asp (RGD) peptide-conjugated AuNSts (RGD-AuNSts) were designed in PA imaging for highly sensitive angiography (Figure 4H & I) [102]. Anti-HER2-conjugated AuNRs with an absorption peak at 810 nm have also been successfully used for cancer detection [103].

Recently, an anisotropic, branched, gold nanoarchitecture of gold tripods with sizes of less than 20 nm

Table 1. Typical exogenous contrast agents for photoacoustic imaging.

Contrast agent	Size (nm)	Peak absorption wavelength/imaging wavelength (nm)	Extinction coefficient (M^{-1} cm^{-1})	Ref.
Gold nanospheres	2–100	520–600	$(3.61 \pm 0.08) \times 10^6$–$(6.06 \pm 0.03) \times 10^9$ (d = 4–40 nm)	[43,86]
Gold nanorods	Diameter of 10–20 by aspect ratio of 2–10	650–1300	$3.3 \pm 0.3 \times 10^9$ (length = 44.8 ± 4.1 nm; width = 19.8 ± 2.9 nm; λ_{peak} = 675 nm) $5.5 \pm 0.3 \times 10^9$ (length = 51.0 ± 4.4 nm; width = 14.1 ± 2.1 nm; λ_{peak} = 850 nm)	[47,53]
Gold nanoshells	50–500	700–2200	8.3×10^9 (diameter = 30.4 ± 4.4 nm; thickness = 7.8 ± 2.2 nm)	[40,87]
Gold nanoprisms	Thickness of 10–40 by planar width of 80–500	700–2000	–	[15]
Gold nanocages	20–500	600–1200	4.34×10^{10} (outer edge length = 45.0 nm; wall thickness = 5.8 nm)	[34,69]
Gold nanostars	Core size of 20–60 by branch length of 10–30	650–900	–	[42]
Gold nanovesicles	200–300	650–1000	–	[38,45]
ICG	<2	618, 668	0.8×10^5–1.8×10^5	[76,88]
Methylene blue	<2	677	7.4×10^4	[77,89]
IRDye® 800CW (Li-Cor Biosciences, NE, USA)	<2	710–890	2.4×10^5	[78,90]
Alexa Fluor® (Life Technologies, CA, USA)	<2	350–790	1.9×10^4–2.6×10^5 (λ_{peak} = 346–782 nm)	[79,91]
SWNTs	1 by 50–300	690	4400 ± 1000	[80,92]
Silver nanoplates	Thickness of 10–30 by planar width of 20–220	550–1100	–	[81]
Gold-coated SWNTs	11 by 100	900	–	[82]
ICG-enhanced SWNTs	1.2 by 150	780	–	[83]
Iron oxide–gold nanoshells	30–40	660–900	–	[84]
MNPs and gold-coated SWNTs	12.8 by 91.7	639, 850	–	[85]

λ_{peak}: Peak wavelength; d: Diameter; ICG: Indocyanine green; MNP: Magnetic nanoparticle; SWNT: Single-walled carbon nanotube.

were shown to have great promise as contrast agents for *in vivo* PA imaging of cancer [104]. Intravenous injection of cyclic Arg–Gly–Asp–D-Phe–Cys peptide-conjugated gold tripods to U87MG tumor-bearing mice showed threefold higher PA imaging contrast than that of the blocking group.

Circulating tumor cell imaging

Death in patients with cancer often results from metastatic spread from the primary tumor, and so the highly sensitive detection of circulating tumor cells would greatly enhance overall patient survival.

The feasibility of using targeted AuNSs to label breast cancer cells in human blood was demonstrated by a PA flow cytometry system with a detection threshold of ten breast cancer cells [105]. AuNSs have also shown the capability of detecting circulating prostate cancer cells [106] and melanoma cells [107] with improved PA effect in a static system over wavelengths of 470–550 nm (with a maximum increase of 41% at 500 nm). Targeting molecules of HER2- and EGFR-conjugated AuNRs with absorption peaks at 800 and 1064 nm were successfully utilized for performing multiplexed imaging of OECM1 oral squamous cell carcinoma cells and Cal27 squamous cell carcinoma cells, respectively [108].

Recently, a AuNP and MNP-based magnetomotive PA (mmPA) imaging technology was reported to greatly increase the sensitivity and specificity of sensing targeted cells or molecular interactions, whose

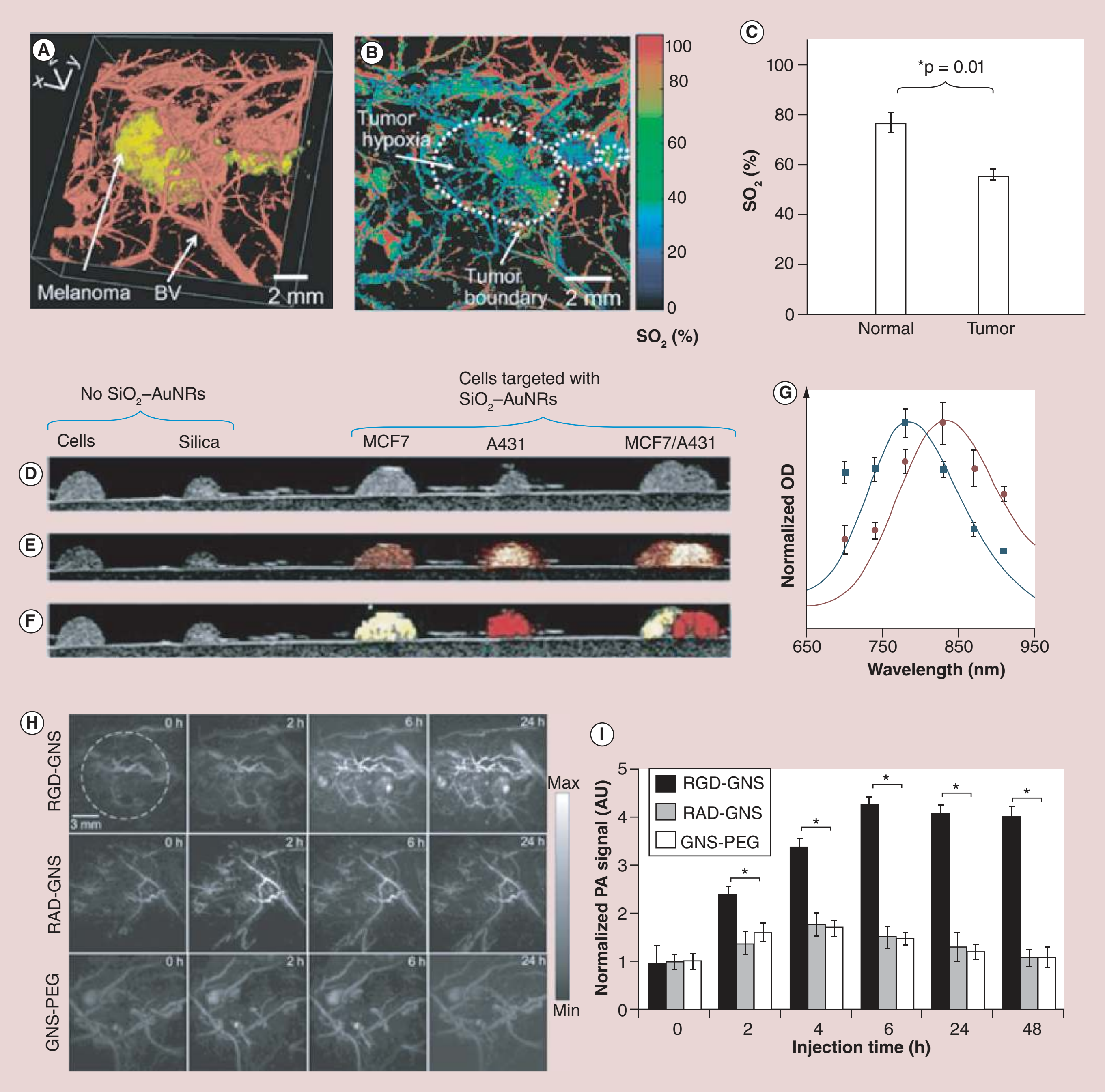

Figure 4. Photoacoustic imaging of tumor vasculature with and without contrast agent. **(A)** Volumetric morphological PA image of B16 melanoma (yellow) and its surrounding blood vessels (BVs; red). The melanoma was imaged using the PA macroscope at 778 nm (ultrasonic frequency = 10 MHz), and the surrounding vasculatures were obtained using a PA microscope at 570 nm (ultrasonic frequency = 50 MHz). **(B)** PA maximum amplitude projection mapping of hemoglobin oxygen saturation (SO_2) of BVs surrounding the melanoma using two optical wavelengths of 564 and 570 nm. The white dotted line shows the tumor boundary. **(C)** Statistical analysis of the average SO_2 in normal mice skins and tumor hypoxic area. **(D)** US, **(E)** US/PA, and **(F)** US/sPA of gelatin phantoms containing cells and two different types of molecularly targeted silica-coated nanorods. **(G)** Distinct absorption spectra of the nanorods used to simultaneously detect the different molecular expressions. PA angiography *in vivo*. **(H)** Sequential PA maximum intensity projection frames captured before, 2, 6, and 24 h postinjection of the RGD-GNS (upper panel), RAD-GNS (middle panel) and GNS-PEG (lower panel) through tail vein. **(I)** Time course of region of interest quantification of PA signal.

*p = 0.01.

AU: Arubitrary unit; AuNR: Gold nanorod; BV: Blood vessel; GNS: Gold nanostar; OD: Optical density; PA: Photoacoustic; RAD: Arg-Ala-Asp; RGD: Arg–Gly–Asp.

primary advantage is the suppression of background signals through magnetic enrichment/manipulation with the simultaneous PA detection of magnetic contrast agent-targeted objects. An example of a composite mmPA contrast agent consists of a MNP with a 25-nm diameter coated with a gold shell (MNP–gold core–shell) with a gap between the MNP core and the AuNSh of approximately 3 nm and a shell thickness of 1–5 nm, whose SPR extinction peak ranged from 660 to 900 nm, enabling maximal light penetration into tissue for PA imaging [84].

Another composite mmPA contrast agent combines a AuNR core with a silica coating layer (Figure 5), which provides a structural scaffold for MNP attachment and increases the PA stability of the AuNR core, whose characteristic SPR peak depends on the AuNRs [109–111]. Results from phantom and *in vitro* studies using these contrast agents demonstrate the capability of mmPA imaging to trap and sensitively detect targeted cells (HeLa cells mimicking circulating tumor cells) at the concentration of a single cell per milliliter of blood [109].

Due to the promises of stem cell therapy for musculoskeletal diseases such as muscular dystrophy, including the regeneration of myofibers, silica-coated AuNRs as contrast agents were recently used for the PA imaging and quantitation of mesenchymal stem cells in rodent muscle tissue, which enabled the imaging of 100,000 cells *in vivo* with a spatial resolution of 340 μm a the temporal resolution of 0.2 s [112]. Moreover, AuNCs as contrast agents were also successfully used to label human mesenchymal stem cells for both *in vitro* and *in vivo* long-term tracking using two-photon microscopy and PA microscopy [96].

Lymph node mapping & cancer cell metastasis imaging

Malignant tumor cells are metastasized through the lymphatic system in most developed cancers; therefore, the reliable detection of metastatic cancer cells in the sentinel lymph node (SLN) can play an important role in diagnosing and treating cancer, and several studies have demonstrated the capability of using AuNP-enhanced PA imaging to map lymph nodes

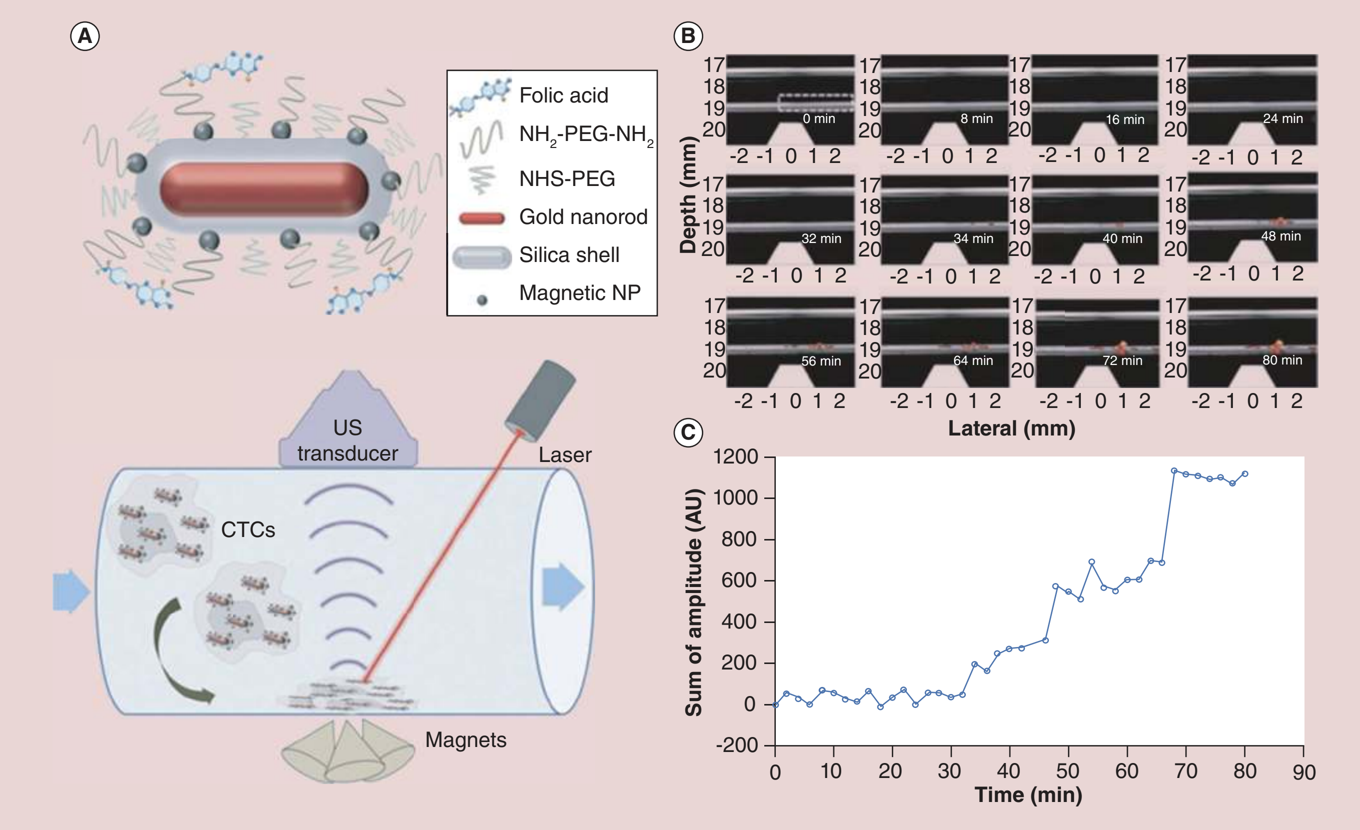

Figure 5. Photoacoustic imaging of circulating tumor cells. (A) Illustrations of the multifunctional nanoparticle and photoacoustic imaging system for CTC detection. Trapping and imaging gold nanorod-silica-magnetic nanoparticle-folic acid labeled HeLa cells at 1 cell ml^{-1} concentration. **(B)** 12 representative time-lapse US/photoacoustic images of the trapped HeLa. **(C)** Total PA signal within the tube region (dashed rectangle in the first frame) plotted as a function of time.
AU: Arbitrary unit; CTC: Circulating tumor cell; NHS: N-hydroxysuccinimide; NP: Nanoparticle; US: Ultrasound.

and identify the metastasis of cancer cells through the lymphatic system.

It was shown that AuNRs could act as lymph node tracers for noninvasive *in vivo* spectroscopic PA SLN mapping in a rat model due to their good biocompatibility, high optical absorption and easily tuned SPR peak wavelength [113]. Gold-coated SWNTs were also shown to be able to identify the SLN in a selected area of the mesenteric region of a mouse [82]. *In vivo* PA imaging was shown to be capable of SLN mapping by using AuNCs as lymph node tracers in a rat model (Figure 6) [114], and the SLN as deep as 33 mm below the skin surface could be imaged with good spatial resolution. Moreover, the principles of PA flow cytometry can be extended to enable *in vivo* assessment of migrating cancer cells within lymphatics, and the utility of AuNRs and AuNShs as cellular markers was demonstrated [115,116]. Recently, AuNSts were also utilized for the PA imaging of the SLN in rats after footpad injection [75], and differential images demonstrate that AuNSts can be used for noninvasive *in vivo* mapping of the lymphatic system.

Imaging of atherosclerotic plaques

When atherosclerotic plaques progress, macrophages are recruited into the arterial wall, then low-density lipoprotein and other debris is phagocytized by macrophages, resulting in foam cell formation and the development of a necrotic core. Therefore, macrophages can provide a logical delivery target for exogenous contrast agents.

Combined intravascular ultrasound (IVUS) and intravascular PA (IVPA) imaging of AuNS-labeled macrophages was demonstrated using both *in vitro* phantom models and *ex vivo* artery samples (Figure 7) [117,118]. Endocytosed AuNSs within atherosclerotic regions were differentiated from colloidal particles by spectroscopic PA imaging, which provides a method for the IVPA imaging of phagocytically active macrophages within atherosclerotic plaques. In addition to the targeting of macrophages as a cellular target for the delivery of exogenous contrast to atherosclerotic lesions, several inflammatory molecular targets have also been explored by using AuNP-based PA imaging. ICAM-1, a biomarker that is overexpressed on the endothelium and macrophages at sites of inflammation, was conjugated with AuNRs for *in vitro* PA imaging [119]. These results were later expanded through the PA imaging of similar anti-VCAM-1-conjugated AuNRs [120] and AuNShs [9] within a mouse inferior vena cava.

Moreover, multiplexed PA imaging was demonstrated *in vitro* by using AuNRs with distinct peaks at 715 and 800 nm conjugated with antibodies against ICAM-1 and E-selectin, which are overexpressed on endothelial cells during inflammation [121]. These results indicate the possibility for PA imaging of AuNP-labeled inflammatory biomarkers for atherosclerosis and suggest the potential for labeling multiple targets by tuning a contrast agent's absorption spectrum and bioconjugation. Recently, Yeager *et al.* [122] demonstrated that PEGylated AuNRs preferentially label atherosclerotic regions and that the AuNRs can be subsequently detected using combined IVUS/IVPA imaging in the presence of luminal blood. Due to the tendency of the AuNRs to extravasate at sites with dysfunctional endothelium, IVPA imaging may be utilized to identify the location of acute inflammation within atherosclerotic plaques.

Brain functional imaging

AuNP-based PA imaging has also been utilized to image brain vasculature and functionality in small animals. This concept was first demonstrated through the intravenous injection of PEGylated AuNShs with silica cores [52] for PA imaging within the NIR region in order to improve contrast of the vasculature of a rat brain relative to background tissue. The images present a gradual enhancement of the optical absorption in the brain vessels by up to 63% after three sequential administrations of AuNShs. By using PEGylated AuNCs as effective NIR contrast agents, the vasculature of the rat brain following the intravenous injection of AuNCs was imaged, the PA images demonstrated that the rat brain vasculature could be imaged with greater clarity and enhanced contrast and the enhancement of blood absorption had a peak value of 81% over the intrinsic contrast at approximately 2 h after the injection, which is better than the 63% enhancement when AuNShs were used at similar doses, due to their more compact sizes and larger optical absorption cross-sections (Figure 8A–D) [66]. Moreover, PEGylated hollow AuNShs (HGNs) with an absorption peak at 800 nm as exogenous agents were also evaluated the through PA imaging of the living nude mice brain vasculature. Images of the mouse brain vasculature after intravenous injection of PEGylated HGNs showed greater clarity and more detailed structures than those without contrast, and brain blood vessels as small as approximately 100 μm in diameter could be clearly seen [123].

Recently, AuNS-based trimodality MRI–PA imaging–Raman imaging NPs have also seen success as diagnostic agents for brain cancer. AuNSs were used not only as PA agents, but also to deliver gadolinium for preoperative MRI detection and surgical planning, as well as to simultaneously deliver PA and Raman imaging agents for delineating tumor margins with at least picomolar sensitivity (Figure 8E & F) [124].

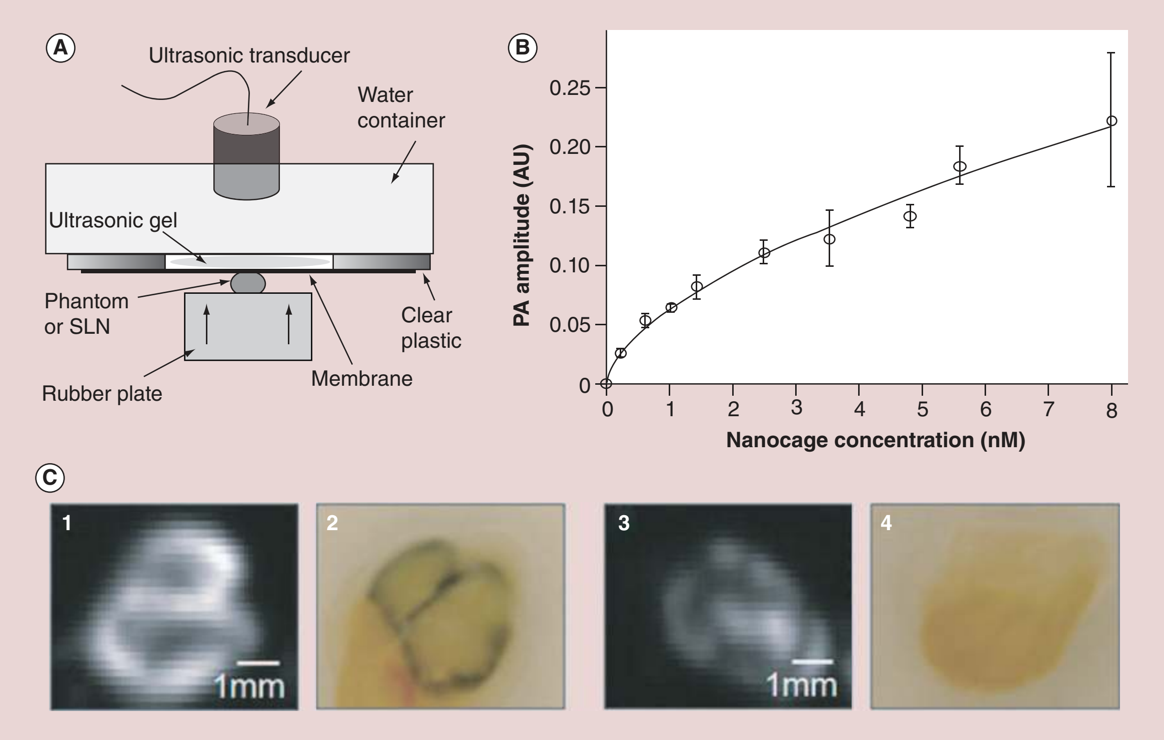

Figure 6. Photoacoustic imaging of sentinel lymph nodes. (A) Experimental setup for PA signal measurements from SLNs and gelatin phantoms containing nanocages. **(B)** PA signal from the gelatin phantom containing nanocages with various concentrations (0-8 nM). All measured values were scaled down to 0 decibel gain. Errorbar indicates standard deviation. **(C)***Ex vivo* photoacoustic images and photographs of dissected SLNs containing Au nanocages for PA signal measurement. A PA image (1) and a corresponding photograph (2) of the highly accumulated SLN. A PA image (3) and a corresponding photography (4) of the low accumulated SLN. In the photographs, dark blue represents the accumulation of nanocages.
Data points and error bars represent in **(B)** are given as means ± standard deviation.
AU: Arbitrary unit; PA: Photoacoustic; SLN: Sentinel lymph node.

AuNP-based PA imaging for therapy guidance

AuNP-based PA imaging has shown potential for aiding therapies by providing sequential monitoring of tumor functional properties, such as changes in tumor vasculature before, during and after therapeutic procedures.

PA imaging can help determine the location of the tumor, monitor heterogeneities in the vasculature within it and monitor the therapeutic agent accumulation. Cui and Yang used PA microscopy to visualize AuNRs accumulated at a tumor site in a mouse model in order to guide the application of high-intensity focused ultrasound for therapy [125]. Taruttis *et al.* demonstrated the real-time imaging of circulating AuNRs in blood vessels in the neck region of a mouse injected with NPs [126]. By using the multispectral technique, a 10 frame per second acquisition system was used for collecting signals from a 64-element ultrasound detector array with the mouse illuminated from multiple directions in order to obtain multiple wavelength images [127]. Golden carbon nanotubes conjugated with an antibody specific to lymphatic endothelial hyaluronan receptor-1 have been used to visualize heterogeneities of endogenous low-absorbing mesenteric structures in nude mice [82]. The PA image provided information on the heterogeneous accumulation of targeted golden carbon nanotubes in order to guide photothermal therapy (PTT) to cause spatially specific thermal damage to the lymphatic walls [82]. It is worth noting that continuous wave lasers are often used for PTT, which are different from those used for PA imaging (i.e., expensive Q-switched lasers). The relatively low optical power of continuous wave lasers delivered to the targeted tissue results in extremely weak acoustic waves and a low signal-to-noise ratio of the detected signals.

The use of AuNPs as drug carriers has been proposed for many applications [128]. Cancer drugs, such as recombinant human TNF [129] and silicon phthalocyanine [130], have been bound to AuNSs; thus, PA imaging with AuNSs as contrast agents could be used to track drug delivery agents in real time. PA imaging can also aid in the customized delivery of drugs with the use of AuNP-based multifunctional NPs. Controlled and customized drug delivery can be realized by using light-triggered nanoconstructs containing the drug paclitaxel encapsulated in hollow AuNSs; the light dose can be adjusted depending on the concentration of hollow AuNSs in the tumor in order to enable sufficient release of paclitaxel [131]. Recently, Ce6-loaded polyethylene oxide-*b*-polystyrene–gold vesicular assemblies were developed for cancer imaging-guided therapy. The strong NIR absorption (650–800 nm) resulted from plasmon coupling between adjacent AuNPs, and the capability of encapsulating active compounds in gold vesicles enabled NIR fluorescence–thermal–PA trimodality imaging-guided synergistic

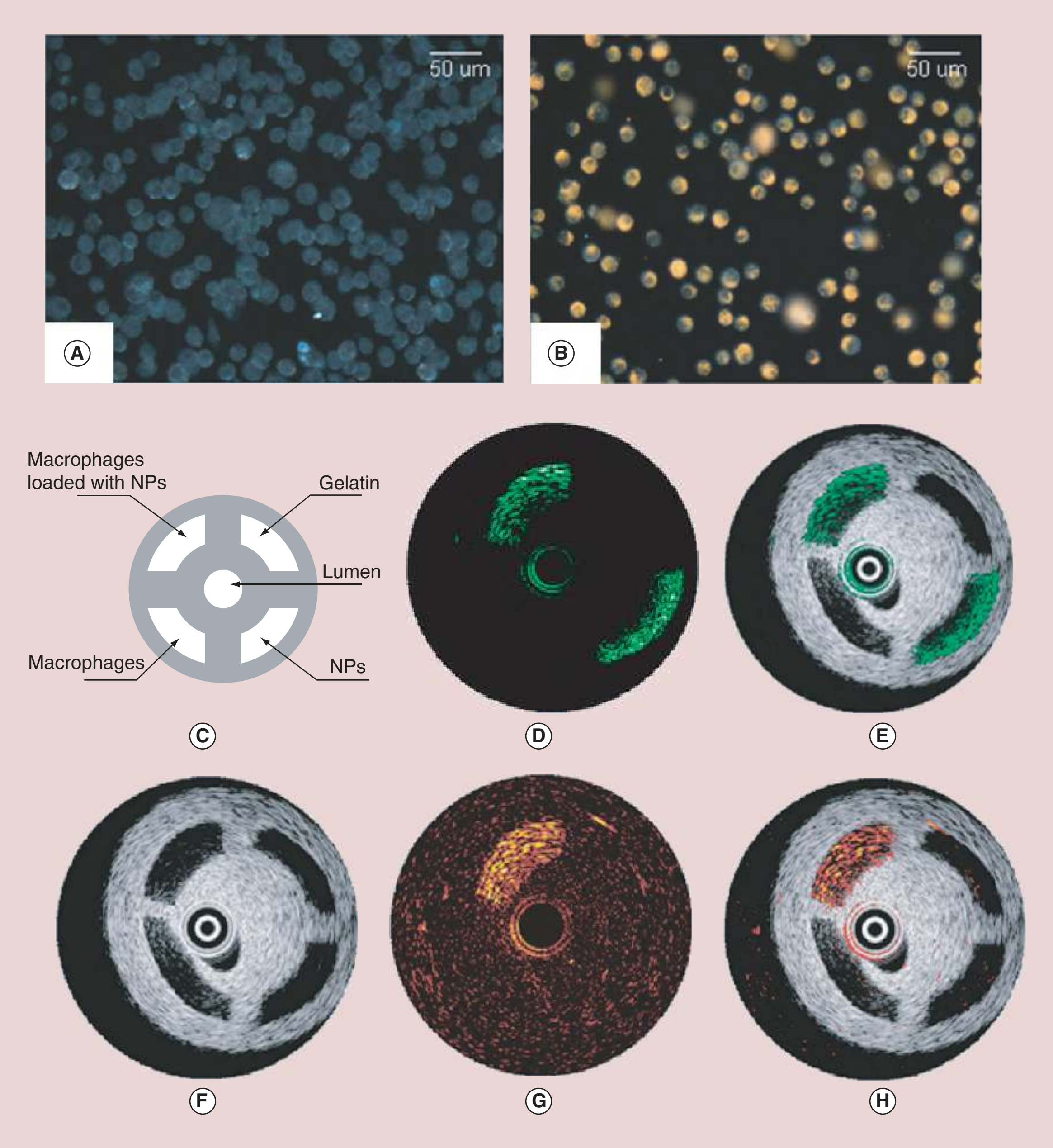

Figure 7. Darkfield reflectance optical images of intact murine macrophages. **(A)** Murine macrophages loaded with gold nanoparticles **(B)**. The diagram **(C)** and the IVUS image **(F)** of the tissue mimicking phantom. The dynamic ranges of IVUS and IVPA images were 50 and 17 decibel, respectively. The IVPA images of the same cross-section of the phantom were taken at 532 nm **(D)** and 680 nm wavelength **(G)**. The combined IVUS and IVPA images of the phantom (**E**; 532 nm wavelength and **H**; 680 nm wavelength) indicate the origin of the PA responses in IVPA images.

IVPA: Intravascular photoacoustic; IVUS: Intravascular ultrasound; NP: Nanoparticle.

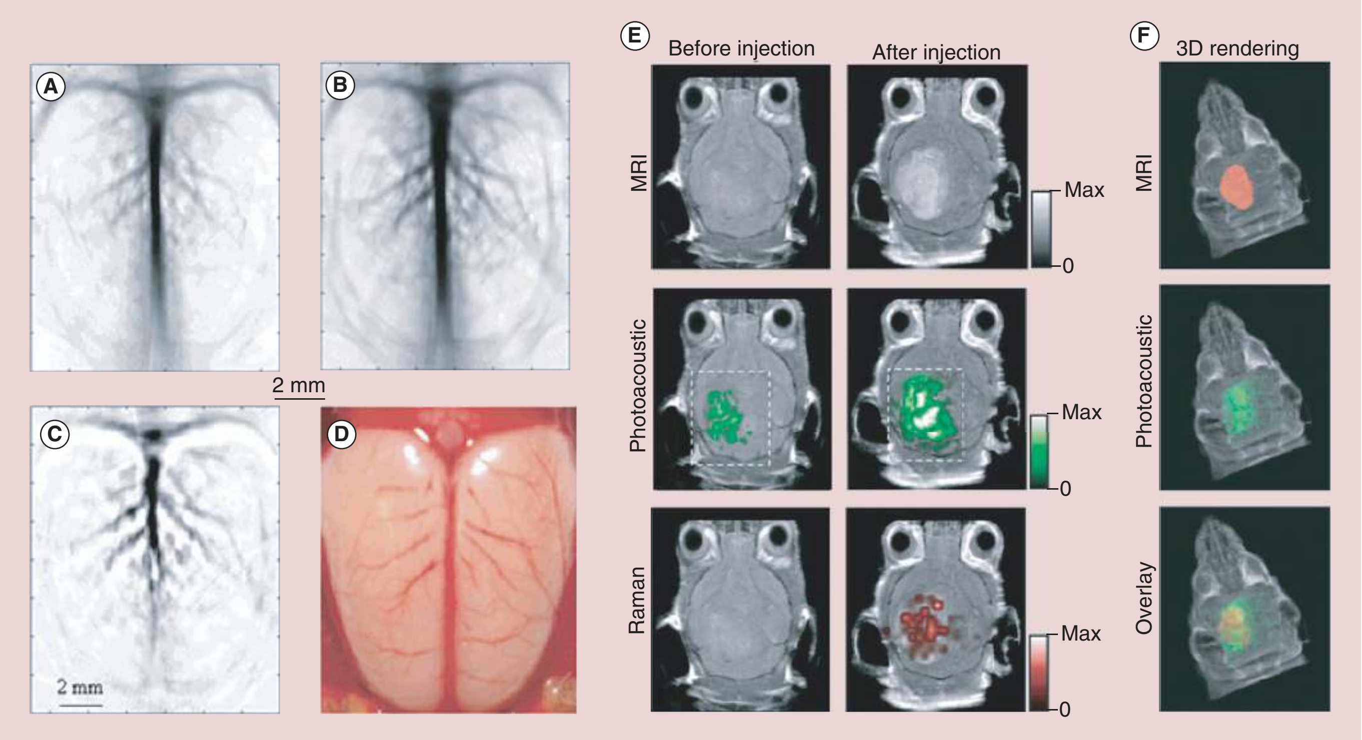

Figure 8. Noninvasive photoacoustic imaging of a rat's cerebral cortex. (A) Before the injection of nanocages and **(B)** about 2 h after the final injection of nanocages, which is the peak enhancement point. **(C)** A pixelwise differential image (image B-image A). **(D)** An openskull photograph of the rat's cerebral cortex. Three successive injections were administrated in these results. Triple-modality detection of brain tumors in living mice with MPRs. **(E)** Two-dimensional axial MRI, PA and Raman images. The postinjection images of all three modalities showed clear tumor visualization (dashed boxes outline the imaged area). **(F)** A 3D rendering of magnetic-resonance images with the tumor segmented (red, top), an overlay of the three-dimensional PA images (green) over the MRI (middle) and an overlay of MRI, the segmented tumor and the PA images (bottom) showing good colocalization of the PA signal with the tumor.
PA: Photoacoustic.

photothermal/photodynamic therapy with improved efficacy [41]. Moreover, Campardelli *et al.* synthesized a stimuli-responsive drug delivery model system by encapsulating NIR-sensitive HGNs together with the molecule to be released into biodegradable polylactic acid (PLA) submicron particles [132]. The rapid heating of the HGNs inside PLA particles caused by NIR radiation enabled the use of the PLA–HGN composites as a phototriggered drug release system. The release rate from the composite particles could be controlled by easily tunable variables, such as HGN load, laser intensity and duration of the NIR irradiation, which makes the composite PLA–HGN submicron particles promising vectors for photothermally controlled drug delivery [132].

AuNPs can also act as PTT agents, while contrast-enhanced PA imaging can be used to monitor the outcome of therapy. This post-therapy image may be compared with the original diagnostic image in order to evaluate the efficacy of treatment, presenting a promising area in the future development of PA imaging. In PTT, efficient optical absorbers are used to heat the tissue to higher temperatures, causing thermal damage. A tumor loaded with AuNRs showed significant temperature elevations in response to laser irradiation [133]. Both PA imaging and ultrasound (US) imaging can be used to obtain temperature maps of the tumor during PTT. PA-based thermal imaging in the presence of strong optical absorbers has a higher signal-to-noise ratio when compared with US-based thermal imaging [134]. Theranostic hollow AuNSs were also examined in an orthotopic glioma model by targeting integrin receptors via RGD peptides, imaging via photoacoustic tomotgraphy and treatment via PTT. Highly specific tumor diagnosis was achieved, and a decrease in tumor volume for up to 3 weeks post-NIR laser treatment was observed [135]. Another theranostic platform based on biodegradable PEG-*b*-poly(ε-caprolactone) block-copolymer graft-capped gold nanovesicles was developed for PA imaging and PTT (Figure 9) [43]. The strong NIR absorption induced by plasmon coupling resulted in high photothermal conversion efficiencies of up to 37%, which enables simultaneous thermal/PA imaging and enhanced PTT efficacy and improved clearance of the dissociated particles after the completion of PTT due to the polycaprolactone melting point of approximately 60°C [43]. One 'on-spot' theranostic platform combining hemispherical PA imaging (HPAI) with RGD–AuNSts was developed in order to image and inhibit tumor angiogenesis and monitor the

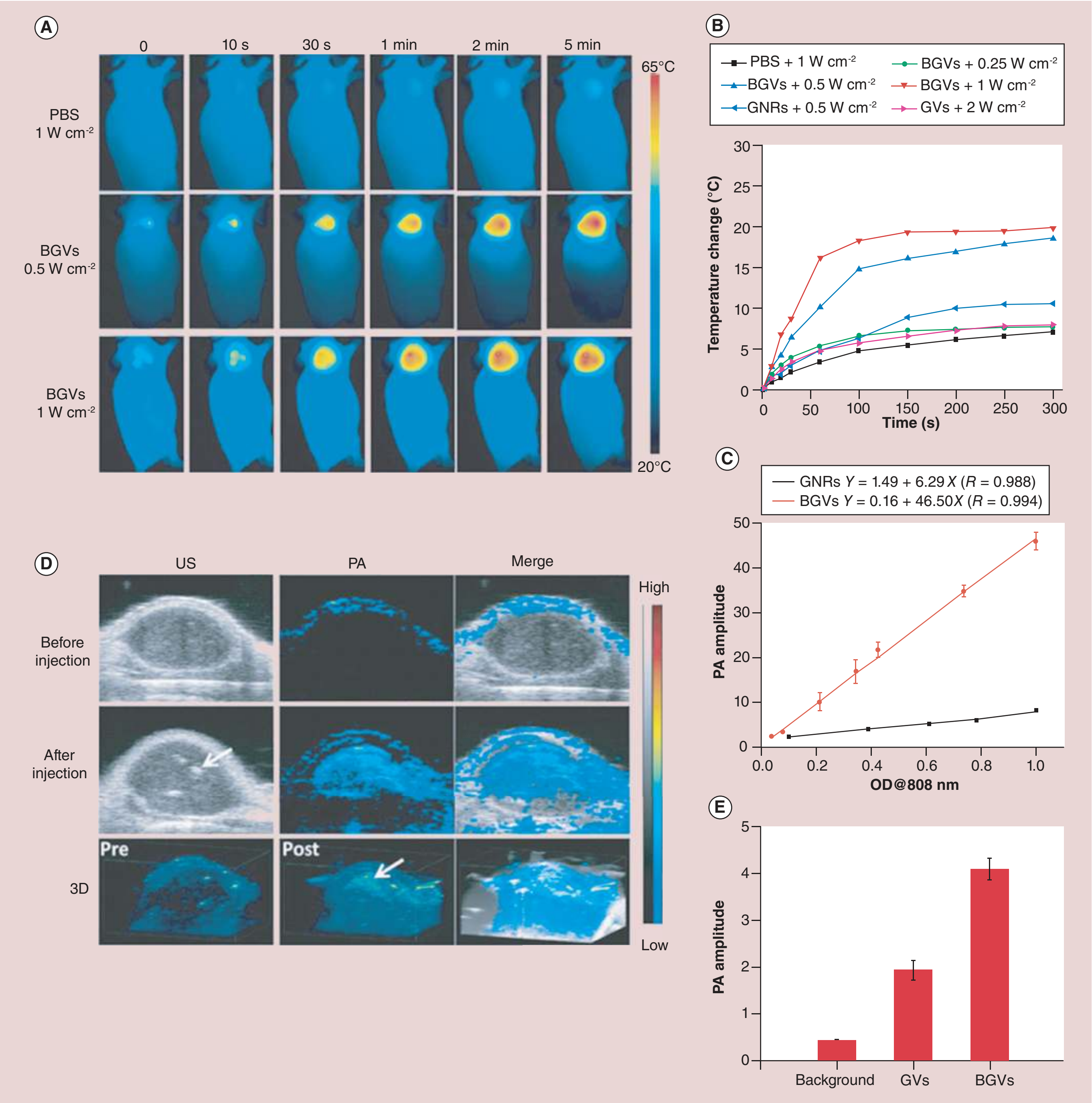

Figure 9. Photothermal and photoacoustic imaging of tumors injected with biodegradable gold nanovesicles. (A) Thermal images of MDA-MB-435 tumor-bearing mice exposed to an 808-nm laser for 5 min after the injection of PBS or BGVs. **(B)** Heat curves of tumors upon laser irradiation as a function of irradiation time. **(C)** PA signals of BGVs and GNRs as a function of optical density. **(D)***In vivo* 2D US and PA images and 3D PA images of tumor tissues before and after the injection of BGVs. Arrows indicate the location of BGVs. **(E)** PA intensities of tumor tissues following the intratumoral administration of the same amount of GVs or BGVs.
Data points and error bars represent in **(B, C & E)** are given as means ± standard deviation.
BGV: Biodegradable gold nanovesicle; GNR: Gold nanorod; GV: Gold vesicle; OD: Optical density; PA: Photoacoustic; PBS: Phosphate-buffered saline; US: Ultrasound.

tumor response [102]. RGD–AuNSt-enhanced HPAI provided the PA signal for tumor neovasculature visualization with high imaging specificity and nanomolar sensitivity. The high absorption-to-scattering ratio of RGD–AuNSts in the NIR region enables photothermal ablation to neovessels in the tumor by laser irradiation, and the therapeutic effect can be noninvasively monitored by HPAI. Recently, IVUS/IVPA imaging has been demonstrated to be a novel imaging modality that is capable of visualizing both the morphology (via IVUS) and cellular/molecular composition (via IVPA) of atherosclerotic plaques by using silica-coated AuNRs as exogenous contrast agents. The IVPA signal intensity of silica-coated AuNRs absorbing within the NIR optical wavelength range is shown to have a linear relationship with temperature change. Therefore, IVUS/IVPA imaging can provide a platform for the detection and temperature monitoring of atherosclerotic plaques through the selective heating of AuNPs [136]. The examples provided in this section clearly indicate the potential of PA imaging with AuNPs as contrast agents for guiding and monitoring therapeutic procedures.

Challenges of AuNP-based PA imaging for biomedical applications

AuNP-based PA imaging holds the promise of becoming a valuable tool in multiple clinical areas due to the inherent and geometrically induced optical properties of AuNPs. In addition to the mentioned advantages, there are still many challenges to overcome.

The SPR peaks of AuNPs can be fine tuned by manipulating their shapes and sizes, among other factors. However, except for AuNSs, AuNRs and AuNCs, the precisely controlled synthesis of other AuNPs with excellent reproducibility still needs to be further improved for wavelength-dependent PA imaging. In the meantime, the issues of scale-up synthesis of AuNPs with good reproducibility that are required for *in vivo* work should also be addressed.

Another concern for PA contrast agents is their photostability. During PA imaging, some plasmonic AuNPs can change their shapes because high laser energies will make anisotropic NPs more spherical [137]. This results in a corresponding shift in the absorption spectra of the particles, resulting in a decreased PA signal and inconsistent images over time. Although the stability of plasmonic NPs can be enhanced by coating them with a thin layer of silica [138], more reliable contrast agents should be developed that retain their efficacy throughout the entire imaging session.

The ability to produce sufficient PA imaging signals or therapeutic efficacies with a relatively low dose of injected AuNPs will also have to be carefully studied. With some agents, insufficient amounts of signal are delivered to the target site(s) because of the limit of the total injectable mass that is nontoxic to the subject.

Due to the photothermal effect as a result of SPR, AuNPs can also act as PTT agents, and PA imaging in order to visualize molecular interactions could be used to monitor the outcomes of therapy, presenting a promising area in the future development of PA imaging. However, typical AuNPs possess relatively low photothermal conversion efficiencies, so it is still necessary to develop more AuNP-based photothermal agents with higher photothermal conversion efficiencies in order to further improve the therapeutic efficacy of PTT.

AuNP-based PA imaging is a rapidly emerging field because of the advantages described earlier. For these NPs to move into the clinic, it is important that more safety studies are conducted for each type of NP. Therefore, AuNP biodistribution, target binding, clearance, potential toxicity and/or interference with other medical tests after administration into the body must be further addressed.

Conclusion & future perspective

PA imaging shows great promise for use in a wide array of medical procedures, ranging from diagnosis to therapy guidance. It can be used to guide common procedures as well as cutting-edge techniques. This versatility, coupled with its real-time and nonionizing nature, promises to make PA imaging a valuable tool in research and in the clinic.

The unique shapes of NPs, ranging from nanospheres, nanoshells, nanorods, nanoprisms, nanocages, nanostars and vesicles, enbue AuNPs with characteristic properties based on their size, symmetry, asymmetry, internal voids and sharp points. In particular, their SPR peaks can be fine tuned by manipulating these characteristics during synthesis. Therefore, the utility of AuNPs in terms of these optical properties, as well as gold's intrinsic properties of photothermal conversion efficiency and biocompatibility, have made AuNPs suitable exogenous contrast agents for PA imaging.

PA imaging with AuNPs as exogenous contrast agents has enabled cellular and molecular imaging and enhanced functional imaging with applications ranging from molecular diagnosis and specific treatment of disease to image-guided delivery and release of targeted nanosized drug carriers for the monitoring of therapy outcome. Due to their distinct and tunable absorption spectra in the tissue optical window (650–1100 nm), AuNPs can be used to identify multiple cell types within heterogeneous tissue, indicating their promising application in multiplexed PA imaging *in vitro* and *in vivo*. Moreover, AuNP-based AuNP–MNP composite NPs and trimodal MRI–PA imaging–Raman imaging NPs can enhance the contrast for PA imaging in combination with other imaging modalities, which show promise for enabling more accurate tumor imag-

Executive summary

Background

- Photoacoustic (PA) imaging is a biomedical imaging modality that provides functional information regarding the cellular and molecular signatures of tissue in real time in the absence of ionizing radiation.
- Due to their strong and tunable optical absorptions as a result of the surface plasmon resonance effect, gold nanoparticles (AuNPs) with different sizes, shapes and surface modifiers have been widely used as PA contrast agents.

PA imaging basics

- PA imaging capitalizes on the PA effect, which is simply the generation of an acoustic wave resulting from the absorption of optical energy.
- The wavelength of laser illumination limits the penetration depth in PA imaging, and the contrast in PA imaging is largely determined by the wavelength-dependent optical absorption coefficient of the photoabsorber.

Plasmonic AuNPs

- By changing the size, shape and internal structure of the AuNPs, the relative magnitude of light being absorbed and scattered can be tuned, and optical absorbing-dominant AuNPs in the near-infrared region are more valuable for PA imaging.
- Typical AuNPs of gold nanospheres, gold nanorods, gold nanoshells, gold nanoprisms, gold nanocages, gold nanostars and gold nanovesicle with distinct and tunable absorption spectra in near-infrared region are suitable for PA imaging.
- Besides the plasmonic AuNPs, there are many other PA contrast agents.

AuNP-based PA diagnostic imaging

- AuNP-based PA imaging is well suited to detecting various types of tumors because these plasmonic AuNPs can be accumulated in tumors through the enhanced permeability and retention effect or be functionalized to accumulate through receptor-mediated binding.
- AuNP-based PA imaging has been demonstrated as a potential means for imaging atherosclerotic plaques through both extravascular and intravascular PA imaging.
- AuNP-based PA imaging has also been utilized for imaging the brain vasculature and functionality in small animals with greatly enhanced contrast and sensitivity.

AuNP-based PA imaging for therapy guidance

- AuNP-based PA imaging can aid with the determination of the location of the tumor, monitor the heterogeneities in the vasculature within it and aid in therapeutic agent accumulation.
- After AuNPs are bound with cancer drugs, PA imaging with AuNPs as contrast agents can be used to track drug delivery agents in real time.
- AuNPs can also act as a photothermal therapy (PTT) agent, and PA imaging in order to visualize molecular interactions could be used to monitor the outcomes of PTT.

Challenges of AuNP-based PA imaging for biomedical applications

- The issues of scale-up synthesis of AuNPs with good reproducibility should be addressed.
- More reliable AuNPs should be developed that retain their efficacy throughout the entire imaging session.
- The ability to produce sufficient PA imaging signals or therapeutic efficacies with a relatively low dose of injected AuNPs will have to be carefully studied.
- AuNP biodistribution, target binding, clearance, potential toxicity and/or interference with other medical tests after administration into the body must be further addressed.

Conclusion & future perspective

- Due to their intrinsic properties of fine-tunable SPR peaks by shape and size, photothermal conversion efficiency and biocompatibility, AuNPs show promise as suitable exogenous contrast agents for PA imaging and image-guided therapy.
- AuNP-based AuNP–magnetic nanoparticle composites and triple-modality MRI–PA imaging–Raman imaging nanoparticles can enhance contrast for PA imaging in combination with other imaging modalities, which show promise for enabling more accurate tumor imaging.
- As AuNPs can also act as cancer drug carriers or PTT agents, AuNP-based PA imaging could be used for the specific treatment of disease through the image-guided delivery and release of targeted drug carriers and the monitoring of therapy outcomes.
- The clinical translation of AuNPs will also be impeded by several fundamental limitations.

ing. AuNPs might also play an important role in PA imaging-assisted treatment modalities.

AuNPs used for molecular PA imaging can also function as drug delivery carriers; thus, drug delivery and release is an active and expanding area of PA imaging with AuNPs as exogenous contrast agents. AuNPs can also act as PTT agents, and PA imaging to visualize molecular interactions could be used to monitor the outcome of therapy, which may be compared with the original diagnostic result in order to evaluate the efficacy of treatment, presenting a promising area in the future development of PA imaging.

Although the clinical translation of AuNPs is still be impeded by some limitations, further developments in tailoring the surface chemistry, morphology and optical properties of AuNPs will open up opportunities for AuNP-based PA imaging in disease detection, treatment surveillance and targeted therapy in a range of pathologies.

Financial & competing interest disclosure

This work was supported in part by the National Basic Research Program of China (973 program, 2013CB733802, 2014CB744503), the National Natural Science Foundation of China (project no. 50902093, 81371596 and 81371645) and the Intramural Research Program (IRP) of the National Institute of Biomedical Imaging and Bioengineering (NIBIB), NIH. The authors have no other relevant affiliations or financial involvement with any organization or entity with a financial interest in or financial conflict with the subject matter or materials discussed in the manuscript apart from those disclosed.

No writing assistance was utilized in the production of this manuscript.

References

Papers of special note have been highlighted as:
• of interest; •• of considerable interest

1 Bell AG. Upon the production of sound by radiant energy. *Am. J. Sci.* 20, 305–324 (1880).

2 Xu M, Wang LV. Photoacoustic imaging in biomedicine. *Rev. Sci. Instrum.* 77(4), 041101 (2006).

3 Harrison T, Ranasinghesagara CJ, Lu H, Mathewson K, Walsh A, Zemp RJ. Combined photoacoustic and ultrasound biomicroscopy. *Opt. Express* 17, 22041–22046 (2009).

4 Niederhauser JJ, Jaeger M, Lemor R, Weber P, Frenz M. Combined ultrasound and optoacoustic system for real-time high-contrast vascular imaging *in vivo*. *IEEE Trans. Med. Imaging* 24(4), 436–440 (2005).

5 Wang LV. Multiscale photoacoustic microscopy and computed tomography. *Nat. Photonics* 3(9), 503–509 (2009).

6 Wang LV, Hu S. Photoacoustic tomography: *in vivo* imaging from organelles to organs. *Science* 335(6075), 1458–1462 (2012).

- **Reviews the state of the art of photoacoustic tomography for both biological and clinical studies and discusses future prospects.**

7 Jain PK, Lee KS, El-Sayed IH, El-Sayed MA. Calculated absorption and scattering properties of gold nanoparticles of different size, shape, and composition: applications in biological imaging and biomedicine. *J. Phys. Chem. B* 110(14), 7238–7248 (2006).

8 Weissleder R. A clearer vision for *in vivo* imaging. *Nat. Biotechnol.* 19, 316–317 (2001).

9 Rouleau L, Berti R, Ng VWK *et al.* VCAM-1-targeting gold nanoshell probe for photoacoustic imaging of atherosclerotic plaque in mice. *Contrast Media Mol. Imaging* 8(1), 27–39 (2013).

10 Smith AM, Mancini MC, Nie S. Bioimaging: second window for *in vivo* imaging. *Nat. Nanotechnol.* 4(11), 710–711 (2009).

11 Sordillo L, Pu Y, Pratavieira S, Budansky Y, Alfano R. Deep optical imaging of tissue using the second and third near-infrared spectral windows. *J. Biomed. Opt.* 19(5), 56004–56004 (2014).

12 Shimizu T, Teranishi T, Hasegawa S, Miyake M. Size evolution of alkanethiol-protected gold nanoparticles by heat treatment in the solid state. *J. Phys. Chem. B* 107(12), 2719–2724 (2003).

13 Ye X, Gao Y, Chen J, Reifsnyder DC, Zheng C, Murray CB. Seeded growth of monodisperse gold nanorods using bromide-free surfactant mixtures. *Nano Lett.* 13(5), 2163–2171 (2013).

14 Oldenburg SJ, Averitt RD, Westcott SL, Halas NJ. Nanoengineering of optical resonances. *Chem. Phys. Lett.* 288(2–4), 243–247 (1998).

15 Ah CS, Yun YJ, Park HJ, Kim W–J, Ha DH, Yun WS. Size-controlled synthesis of machinable single crystalline gold nanoplates. *Chem. Mater.* 17(22), 5558–5561 (2005).

16 Wang Y, Liu Y, Luehmann H *et al.* Evaluating the pharmacokinetics and *in vivo* cancer targeting capability of au nanocages by positron emission tomography imaging. *ACS Nano* 6(7), 5880–5888 (2012).

17 Nehl CL, Liao H, Hafner JH. Optical properties of star-shaped gold nanoparticles. *Nano Lett.* 6(4), 683–688 (2006).

18 Wang S, Huang P, Nie L *et al.* Single continuous wave laser induced photodynamic/plasmonic photothermal therapy using photosensitizer-functionalized gold nanostars. *Adv. Mater.* 25(22), 3055–3061 (2013).

19 Personick ML, Langille MR, Zhang J, Harris N, Schatz GC, Mirkin CA. Synthesis and isolation of {110}-faceted gold bipyramids and rhombic dodecahedra. *J. Am. Chem. Soc.* 133(16), 6170–6173 (2011).

20 Emelianov SY, Aglyamov SR, Karpiouk AB *et al.* 1E-5 synergy and applications of combined ultrasound, elasticity, and photoacoustic imaging (invited). Presented at: *IEEE Ultrasonics Symposium 2006*. Vancouver, BC, Canada, 3–6 October 2006.

21 Vo-Dinh T. *Biomedical Photonics Handbook*. CRC Press, FL, USA (2010).

22 Oraevsky AA, Jacques SL, Tittel FK. Measurement of tissue optical properties by time-resolved detection of laser-induced transient stress. *Appl. Opt.* 36(1), 402–415 (1997).

23 Oraevsky AA, Esenaliev RO, Jacques SL, Thomsen SL, Tittel FK. Lateral and z-axial resolution in laser optoacoustic imaging with ultrasonic transducers. *Proc. SPIE* 2389, 198–208 (1995).

24 Kim C, Erpelding TN, Jankovic L, Pashley MD, Wang LV. Deeply penetrating *in vivo* photoacoustic imaging using a clinical ultrasound array system. *Biomed. Opt. Express* 1(1), 278–284 (2010).

25 Esenaliev RO, Karabutov AA, Oraevsky AA. Sensitivity of laser opto-acoustic imaging in detection of small deeply embedded tumors. *IEEE J. Sel. Top. Quant.* 5(4), 981–988 (1999).

26 Ku G, Wang LV. Deeply penetrating photoacoustic tomography in biological tissues enhanced with an optical contrast agent. *Opt. Lett.* 30(5), 507–509 (2005).

27 American National Standards Institute, Laser Institute of America. *American National Standard for the Safe Use of Lasers*. American National Standards Institute, Washington, DC, USA (2000).

28 Zhang HF, Maslov K, Stoica G, Wang LV. Functional photoacoustic microscopy for high-resolution and noninvasive *in vivo* imaging. *Nat. Biotechnol.* 24(7), 848–851 (2006).

29 Maslov K, Zhang HF, Hu S, Wang LV. Optical-resolution photoacoustic microscopy for *in vivo* imaging of single capillaries. *Opt. Lett.* 33(9), 929–931 (2008).

30 Mallidi S, Aglyamov S, Karpiouk A, Park S, Emelianov S. Functional and morphological ultrasonic biomicroscopy for tissue engineers. *Proc. SPIE* 6147, Y1–Y7 (2006).

31 Manohar S, Vaartjes SE, Van Hespen JC *et al.* Initial results of *in vivo* non-invasive cancer imaging in the human breast using near-infrared photoacoustics. *Opt. Express* 15(19), 12277–12285 (2007).

32 Kelly KL, Coronado E, Zhao LL, Schatz GC. The optical properties of metal nanoparticles: the influence of size, shape, and dielectric environment. *J. Phys. Chem. B* 107(3), 668–677 (2003).

33 Mayer KM, Hafner JH. Localized surface plasmon resonance sensors. *Chem. Rev.* 111(6), 3828–3857 (2011).

34 Cho EC, Kim C, Zhou F *et al.* Measuring the optical absorption cross sections of Au–Ag nanocages and au nanorods by photoacoustic imaging. *J. Phys. Chem. C* 113(21), 9023–9028 (2009).

•• **Provides a technique to measure the absorption cross-section (σa) and overall extinction cross-section, and then obtain the scattering cross-section and the contributions of absorption cross-section and scattering cross-section to the optical properties of gold nanostructures.**

35 Myroshnychenko V, Rodríguez-Fernández J, Pastoriza-Santos I *et al.* Modelling the optical response of gold nanoparticles. *Chem. Soc. Rev.* 37(9), 1792–1805 (2008).

36 Grzelczak M, Pérez-Juste J, Mulvaney P, Liz-Marzán LM. Shape control in gold nanoparticle synthesis. *Chem. Soc. Rev.* 37(9), 1783–1791 (2008).

37 Xia Y, Xiong Y, Lim B, Skrabalak SE. Shape-controlled synthesis of metal nanocrystals: simple chemistry meets complex physics? *Angew. Chem. Int. Ed.* 48(1), 60–103 (2009).

38 Link S, El-Sayed MA. Spectral properties and relaxation dynamics of surface plasmon electronic oscillations in gold and silver nanodots and nanorods. *J. Phys. Chem. B* 103(40), 8410–8426 (1999).

39 Xia Y, Li W, Cobley CM *et al.* Gold nanocages: from synthesis to theranostic applications. *Acc. Chem. Res.* 44(10), 914–924 (2011).

40 Gao B, Rozin MJ, Tao AR. Plasmonic nanocomposites: polymer-guided strategies for assembling metal nanoparticles. *Nanoscale* 5(13), 5677–5691 (2013).

41 Lin J, Wang S, Huang P *et al.* Photosensitizer-loaded gold vesicles with strong plasmonic coupling effect for imaging-guided photothermal/photodynamic therapy. *ACS Nano* 7(6), 5320–5329 (2013).

42 He J, Huang X, Li Y-C *et al.* Self-assembly of amphiphilic plasmonic micelle-like nanoparticles in selective solvents. *J. Am. Chem. Soc.* 135(21), 7974–7984 (2013).

43 Huang P, Lin J, Li W *et al.* Biodegradable gold nanovesicles with an ultrastrong plasmonic coupling effect for photoacoustic imaging and photothermal therapy. *Angew. Chem. Int. Ed.* 125(52), 14208–14214 (2013).

• **Reports on a novel theranostic platform based on biodegradable plasmonic gold nanovesicles with tunable localized surface plasmon resonance peaks in the near-infrared region for photoacoustic imaging and enhanced photothermal therapy.**

44 Nikoobakht B, El-Sayed MA. Preparation and growth mechanism of gold nanorods (NRs) using seed-mediated growth method. *Chem. Mater.* 15(10), 1957–1962 (2003).

45 Zhu J, Yong K-T, Roy I *et al.* Additive controlled synthesis of gold nanorods (GNRs) for two-photon luminescence imaging of cancer cells. *Nanotechnology* 21(28), 285106 (2010).

46 Huang X, Neretina S, El-Sayed MA. Gold nanorods: from synthesis and properties to biological and biomedical applications. *Adv. Mater.* 21(48), 4880–4910 (2009).

47 Lee K-S, El-Sayed MA. Dependence of the enhanced optical scattering efficiency relative to that of absorption for gold metal nanorods on aspect ratio, size, end-cap shape, and medium refractive index. *J. Phys. Chem. B* 109(43), 20331–20338 (2005).

48 Wiesner J, Wokaun A. Anisometric gold colloids. Preparation, characterization, and optical properties. *Chem. Phys. Lett.* 157(6), 569–575 (1989).

49 Huang X, El-Sayed IH, Qian W, El-Sayed MA. Cancer cell imaging and photothermal therapy in the near-infrared region by using gold nanorods. *J. Am. Chem. Soc.* 128(6), 2115–2120 (2006).

50 Jokerst JV, Cole AJ, Van De Sompel D, Gambhir SS. Gold nanorods for ovarian cancer detection with photoacoustic

imaging and resection guidance via Raman imaging in living mice. *ACS Nano* 6(11), 10366–10377 (2012).

51 Orendorff CJ, Murphy CJ. Quantitation of metal content in the silver-assisted growth of gold nanorods. *J. Phys. Chem. B* 110(9), 3990–3994 (2006).

52 Wang Y, Xie X, Wang X *et al.* Photoacoustic tomography of a nanoshell contrast agent in the *in vivo* rat brain. *Nano Lett.* 4(9), 1689–1692 (2004).

53 Xiang L, Xing D, Gu H, Yang D, Zeng L, Yang S. Gold nanoshell-based photoacoustic imaging application in biomedicine. Presented at: *2006 International Symposium on Biophotonics, Nanophotonics and Metamaterials*. Hangzhou, China, 16–18 October 2006.

54 Averitt R, Sarkar D, Halas N. Plasmon resonance shifts of Au-coated Au 2 S nanoshells: insight into multicomponent nanoparticle growth. *Phys. Rev. Lett.* 78(22), 4217 (1997).

55 Westcott SL, Oldenburg SJ, Lee TR, Halas N. Construction of simple gold nanoparticle aggregates with controlled plasmon–plasmon interactions. *Chem. Phys. Lett.* 300(5), 651–655 (1999).

56 Westcott SL, Oldenburg SJ, Lee TR, Halas NJ. Formation and adsorption of clusters of gold nanoparticles onto functionalized silica nanoparticle surfaces. *Langmuir* 14(19), 5396–5401 (1998).

57 Oldenburg SJ, Jackson JB, Westcott SL, Halas N. Infrared extinction properties of gold nanoshells. *Appl. Phys. Lett.* 75(19), 2897–2899 (1999).

58 Lin A, Hirsch L, Lee M-H *et al.* Nanoshell-enabled photonics-based imaging and therapy of cancer. *Technol. Cancer Res. Treat.* 3(1), 33–40 (2004).

59 Sun Y, Mayers BT, Xia Y. Template-engaged replacement reaction: a one-step approach to the large-scale synthesis of metal nanostructures with hollow interiors. *Nano Lett.* 2(5), 481–485 (2002).

60 Cole JR, Mirin NA, Knight MW, Goodrich GP, Halas NJ. Photothermal efficiencies of nanoshells and nanorods for clinical therapeutic applications. *J. Phys. Chem. C* 113(28), 12090–12094 (2009).

61 Millstone JE, Hurst SJ, Métraux GS, Cutler JI, Mirkin CA. Colloidal gold and silver triangular nanoprisms. *Small* 5(6), 646–664 (2009).

62 Malikova N, Pastoriza-Santos I, Schierhorn M, Kotov NA, Liz-Marzán LM. Layer-by-layer assembled mixed spherical and planar gold nanoparticles: control of interparticle interactions. *Langmuir* 18(9), 3694–3697 (2002).

63 Millstone JE, Park S, Shuford KL, Qin L, Schatz GC, Mirkin CA. Observation of a quadrupole plasmon mode for a colloidal solution of gold nanoprisms. *J. Am. Chem. Soc.* 127(15), 5312–5313 (2005).

64 Millstone JE, Métraux GS, Mirkin CA. Controlling the edge length of gold nanoprisms via a seed-mediated approach. *Adv. Funct. Mater.* 16(9), 1209–1214 (2006).

65 Skrabalak SE, Chen J, Sun Y *et al.* Gold nanocages: synthesis, properties, and applications. *Acc. Chem. Res.* 41(12), 1587–1595 (2008).

66 Yang X, Skrabalak SE, Li Z-Y, Xia Y, Wang LV. Photoacoustic tomography of a rat cerebral cortex *in vivo* with Au nanocages as an optical contrast agent. *Nano Lett.* 7(12), 3798–3802 (2007).

67 Mahmoud M, El-Sayed M. Metallic double shell hollow nanocages: the challenges of their synthetic techniques. *Langmuir* 28(9), 4051–4059 (2012).

68 Chen J, Saeki F, Wiley BJ *et al.* Gold nanocages: bioconjugation and their potential use as optical imaging contrast agents. *Nano Lett.* 5(3), 473–477 (2005).

69 Yavuz MS, Cheng Y, Chen J *et al.* Gold nanocages covered by smart polymers for controlled release with near-infrared light. *Nat. Mater.* 8(12), 935–939 (2009).

70 Yuan H, Khoury CG, Hwang H, Wilson CM, Grant GA, Vo-Dinh T. Gold nanostars: surfactant-free synthesis, 3D modelling, and two-photon photoluminescence imaging. *Nanotechnology* 23(7), 075102 (2012).

71 Guerrero-Martínez A, Barbosa S, Pastoriza-Santos I, Liz-Marzán LM. Nanostars shine bright for you: colloidal synthesis, properties and applications of branched metallic nanoparticles. *Curr. Opin. Colloid Interface Sci.* 16(2), 118–127 (2011).

72 Kumar PS, Pastoriza-Santos I, Rodriguez-Gonzalez B, De Abajo FJG, Liz-Marzan LM. High-yield synthesis and optical response of gold nanostars. *Nanotechnology* 19(1), 015606 (2008).

73 Hao E, Bailey RC, Schatz GC, Hupp JT, Li S. Synthesis and optical properties of 'branched' gold nanocrystals. *Nano Lett.* 4(2), 327–330 (2004).

74 Khoury CG, Vo-Dinh T. Gold nanostars for surface-enhanced Raman scattering: synthesis, characterization and optimization. *J. Phys. Chem. C* 112(48), 18849–18859 (2008).

75 Kim C, Song H-M, Cai X, Yao J, Wei A, Wang LV. *In vivo* photoacoustic mapping of lymphatic systems with plasmon-resonant nanostars. *J. Mater. Chem.* 21(9), 2841–2844 (2011).

76 Kim G, Huang S-W, Day KC *et al.* Indocyanine-green-embedded PEBBLEs as a contrast agent for photoacoustic imaging. *J. Biomed. Opt.* 12(4), 044020 (2007).

77 Song KH, Margenthaler JA, Wang LV, Stein EW. Noninvasive photoacoustic identification of sentinel lymph nodes containing methylene blue *in vivo* in a rat model. *J. Biomed. Opt.* 13(5), 054033 (2008).

78 Li M-L, Oh J-T, Xie X *et al.* Simultaneous molecular and hypoxia imaging of brain tumors *in vivo* using spectroscopic photoacoustic tomography. *Proc. IEEE* 96(3), 481–489 (2008).

79 Bhattacharyya S, Wang S, Reinecke D, Kiser Jr W, Kruger RA, Degrado TR. Synthesis and evaluation of near-infrared (NIR) dye–herceptin conjugates as photoacoustic computed tomography (PCT) probes for HER2 expression in breast cancer. *Bioconjug. Chem.* 19(6), 1186–1193 (2008).

80 De La Zerda A, Zavaleta C, Keren S *et al.* Carbon nanotubes as photoacoustic molecular imaging agents in living mice. *Nat. Nanotechnol.* 3(9), 557–562 (2008).

81 Homan KA, Souza M, Truby R *et al.* Silver nanoplate contrast agents for *in vivo* molecular photoacoustic imaging. *ACS Nano* 6(1), 641–650 (2012).

82 Kim J-W, Galanzha EI, Shashkov EV, Moon H-M, Zharov VP. Golden carbon nanotubes as multimodal photoacoustic and photothermal high-contrast molecular agents. *Nat. Nanotechnol.* 4(10), 688–694 (2009).

83 Zerda ADL, Liu Z, Bodapati S *et al.* Ultrahigh sensitivity carbon nanotube agents for photoacoustic molecular imaging in living mice. *Nano Lett.* 10(6), 2168–2172 (2010).

84 Jin Y, Jia C, Huang S-W, O'donnell M, Gao X. Multifunctional nanoparticles as coupled contrast agents. *Nat. Commun.* 1, 41 (2010).

85 Galanzha EI, Kokoska MS, Shashkov EV, Kim JW, Tuchin VV, Zharov VP. *In vivo* fiber-based multicolor photoacoustic detection and photothermal purging of metastasis in sentinel lymph nodes targeted by nanoparticles. *J. Biophotonics* 2(8–9), 528–539 (2009).

86 Liu X, Atwater M, Wang J, Huo Q. Extinction coefficient of gold nanoparticles with different sizes and different capping ligands. *Colloids Surf. B Biointerfaces* 58(1), 3–7 (2007).

87 Melancon MP, Lu W, Yang Z *et al. In vitro* and *in vivo* targeting of hollow gold nanoshells directed at epidermal growth factor receptor for photothermal ablation therapy. *Mol. Cancer Ther.* 7(6), 1730–1739 (2008).

88 Oregon Medical Laser Center. Optical absorption of indocyanine green.
http://omlc.org/spectra/icg/index.html

89 Orgeon Medical Laser Center. Optical absorption of methylene blue.
http://omlc.org/spectra/mb/index.html

90 LI-COR. IRDye® 800CW NHS ester: optical properties and structure.
www.licor.com/clinical_translation/irdye_800CW_NHS

91 Life Technologies. The Alexa Fluor dye series.
www.lifetechnologies.com/cn/zh/home/references

92 Schöppler F, Mann C, Hain TC *et al.* Molar extinction coefficient of single-wall carbon nanotubes. *J. Phys. Chem. C* 115(30), 14682–14686 (2011)

93 Laufer J, Zhang E, Beard P. Evaluation of absorbing chromophores used in tissue phantoms for quantitative photoacoustic spectroscopy and imaging. *IEEE J. Sel. Top. Quant.* 16(3), 600–607 (2010).

94 Zhang Q, Iwakuma N, Sharma P *et al.* Gold nanoparticles as a contrast agent for *in vivo* tumor imaging with photoacoustic tomography. *Nanotechnology* 20(39), 395102 (2009).

95 Kim C, Cho EC, Chen J *et al. In vivo* molecular photoacoustic tomography of melanomas targeted by bioconjugated gold nanocages. *ACS Nano* 4(8), 4559–4564 (2010).

96 Zhang YS, Wang Y, Wang L *et al.* Labeling human mesenchymal stem cells with gold nanocages for *in vitro* and *in vivo* tracking by two-photon microscopy and photoacoustic microscopy. *Theranostics* 3(8), 532 (2013).

97 Kim S, Chen Y-S, Luke GP, Emelianov SY. *In vivo* three-dimensional spectroscopic photoacoustic imaging for monitoring nanoparticle delivery. *Biomed. Opt. Express* 2(9), 2540–2550 (2011).

98 Bao C, Beziere N, Del Pino P *et al.* Gold nanoprisms as optoacoustic signal nanoamplifiers for *in vivo* bioimaging of gastrointestinal cancers. *Small* 9(1), 68–74 (2013).

99 Bayer CL, Chen Y-S, Kim S, Mallidi S, Sokolov K, Emelianov S. Multiplex photoacoustic molecular imaging using targeted silica-coated gold nanorods. *Biomed. Opt. Express* 2(7), 1828–1835 (2011).

- **Describes the use of tunable targeted silica-coated gold nanorods with different peak absorption wavelengths as contrast agents for multiplex photoacoustic molecular imaging.**

100 Bayer CL, Chen Y-S, Kim S, Mallidi S, Sokolov K, Emelianov S. Molecular diagnosis of cancer using multiplex photoacoustic imaging with targeted nanorods. Presented at: *IEEE Ultrasonics Symposium 2010*. San Diego, CA, USA, 11–14 October 2010.

101 Li P-C, Wei C-W, Liao C-K *et al.* Photoacoustic imaging of multiple targets using gold nanorods. *IEEE Trans. Ultrason. Ferr.* 54(8), 1642–1647 (2007).

102 Nie L, Wang S, Wang X *et al. In vivo* volumetric photoacoustic molecular angiography and therapeutic monitoring with targeted plasmonic nanostars. *Small* 10(8), 1585–1593 (2013).

103 Agarwal A, Huang SW, O'Donnell M *et al.* Targeted gold nanorod contrast agent for prostate cancer detection by photoacoustic imaging. *J. Appl. Phys.* 102(6), 064701 (2007).

104 Cheng K, Kothapalli S-R, Liu H *et al.* Construction and validation of nano gold tripods for molecular imaging of living subjects. *J. Am. Chem. Soc.* 136(9), 3560–3571 (2014).

105 Thomas T, Dale P, Weight R, Atasoy U, Magee J, Viator J. Photoacoustic detection of breast cancer cells in human blood. *Proc. SPIE* 4856, 685609 (2008).

106 Viator JA, Gupta S, Goldschmidt BS *et al.* Gold nanoparticle mediated detection of prostate cancer cells using photoacoustic flowmetry with optical reflectance. *J. Biomed. Nanotechnol.* 6(2), 187–191 (2010).

107 McCormack DR, Bhattacharyya K, Kannan R, Katti K, Viator JA. Enhanced photoacoustic detection of melanoma cells using gold nanoparticles. *Lasers Surg. Med.* 43(4), 333–338 (2011).

108 Li PC, Wang CR, Shieh DB *et al. In vivo* photoacoustic molecular imaging with simultaneous multiple selective targeting using antibody-conjugated gold nanorods. *Opt. Express* 16(23), 18605–18615 (2008).

109 Hu X, Wei CW, Xia J, Pelivanov I, O'Donnell M, Gao X. Trapping and photoacoustic detection of CTCs at the single cell per milliliter level with magneto-optical coupled nanoparticles. *Small* 9(12), 2046–2052 (2013).

110 Truby RL, Emelianov SY, Homan KA. Ligand-mediated self-assembly of hybrid plasmonic and superparamagnetic nanostructures. *Langmuir* 29(8), 2465–2470 (2013).

111 Chen L-C, Wei C-W, Souris JS *et al.* Enhanced photoacoustic stability of gold nanorods by silica matrix confinement. *J. Biomed. Opt.* 15(1), 016010 (2010).

112 Jokerst JV, Thangaraj M, Kempen PJ, Sinclair R, Gambhir SS. Photoacoustic imaging of mesenchymal stem cells in living mice via silica-coated gold nanorods. *ACS Nano* 6(7), 5920–5930 (2012).

113 Song KH, Kim C, Maslov K, Wang LV. Noninvasive *in vivo* spectroscopic nanorod-contrast photoacoustic mapping

of sentinel lymph nodes. *Eur. J. Radiol.* 70(2), 227–231 (2009).

114 Song KH, Kim C, Cobley CM, Xia Y, Wang LV. Near-infrared gold nanocages as a new class of tracers for photoacoustic sentinel lymph node mapping on a rat model. *Nano Lett.* 9(1), 183–188 (2008).

115 Galanzha EI, Shashkov EV, Tuchin VV, Zharov VP. *In vivo* multispectral, multiparameter, photoacoustic lymph flow cytometry with natural cell focusing, label-free detection and multicolor nanoparticle probes. *Cytometry A* 73(10), 884–894 (2008).

116 Galanzha EI, Tuchin VV, Zharov VP. Advances in small animal mesentery models for *in vivo* flow cytometry, dynamic microscopy, and drug screening. *World J. Gastroenterol.* 13(2), 192–218 (2007).

117 Wang B, Joshi P, Sapozhnikova V *et al.* Intravascular photoacoustic imaging of macrophages using molecularly targeted gold nanoparticles. *Proc. SPIE* 7564, 75640A (2010).

118 Wang B, Yantsen E, Larson T *et al.* Plasmonic intravascular photoacoustic imaging for detection of macrophages in atherosclerotic plaques. *Nano Lett.* 9(6), 2212–2217 (2008).

119 Kim K, Huang S-W, Ashkenazi S *et al.* Photoacoustic imaging of early inflammatory response using gold nanorods. *Appl. Phys. Lett.* 90(22), 223901 (2007).

120 O'Donnell M, Mcveigh ER, Strauss HW *et al.* Multi-modality cardiovascular molecular imaging technology. *J. Nucl. Med.* 51(Suppl. 1), 38S–50S (2010).

121 Ha S, Carson A, Agarwal A, Kotov NA, Kim K. Detection and monitoring of the multiple inflammatory responses by photoacoustic molecular imaging using selectively targeted gold nanorods. *Biomed. Opt. Express* 2(3), 645–657 (2011).

122 Yeager D, Karpiouk A, Wang B *et al.* Intravascular photoacoustic imaging of exogenously labeled atherosclerotic plaque through luminal blood. *J. Biomed. Opt.* 17(10), 106016–106016 (2012).

123 Lu W, Huang Q, Ku G *et al.* Photoacoustic imaging of living mouse brain vasculature using hollow gold nanospheres. *Biomaterials* 31(9), 2617–2626 (2010).

124 Kircher MF, De La Zerda A, Jokerst JV *et al.* A brain tumor molecular imaging strategy using a new triple-modality MRI–photoacoustic–Raman nanoparticle. *Nat. Med.* 18(5), 829–834 (2012).

125 Cui H, Yang X. *In vivo* imaging and treatment of solid tumor using integrated photoacoustic imaging and high intensity focused ultrasound system. *Med. Phys.* 37(9), 4777–4781 (2010).

126 Taruttis A, Herzog E, Razansky D, Ntziachristos V. Real-time imaging of cardiovascular dynamics and circulating gold nanorods with multispectral optoacoustic tomography. *Opt. Express* 18(19), 19592–19602 (2010).

127 Razansky D, Baeten J, Ntziachristos V. Sensitivity of molecular target detection by multispectral optoacoustic tomography (MSOT). *Med. Phys.* 36(3), 939–945 (2009).

128 Malam Y, Loizidou M, Seifalian AM. Liposomes and nanoparticles: nanosized vehicles for drug delivery in cancer. *Trends Pharmacol. Sci.* 30(11), 592–599 (2009).

129 Paciotti GF, Myer L, Weinreich D *et al.* Colloidal gold: a novel nanoparticle vector for tumor directed drug delivery. *Drug Deliv.* 11(3), 169–183 (2004).

130 Cheng Y, C. Samia A, Meyers JD, Panagopoulos I, Fei B, Burda C. Highly efficient drug delivery with gold nanoparticle vectors for *in vivo* photodynamic therapy of cancer. *J. Am. Chem. Soc.* 130(32), 10643–10647 (2008).

131 You J, Shao R, Wei X, Gupta S, Li C. Near-infrared light triggers release of paclitaxel from biodegradable microspheres: photothermal effect and enhanced antitumor activity. *Small* 6(9), 1022–1031 (2010).

132 Campardelli R, Della Porta G, Gomez L, Irusta S, Reverchon E, Santamaria J. Au–PLA nanocomposites for photothermally controlled drug delivery. *J. Mater. Chem. B* 2(4), 409–417 (2014).

- **Demonstrates that the drug release rate from the polylactic acid–hollow gold nanoshell composite particles could be controlled by easily tunable variables of hollow gold nanoshell load, laser intensity and the duration of the near-infrared irradiation.**

133 Mallidi S, Luke GP, Emelianov S. Photoacoustic imaging in cancer detection, diagnosis, and treatment guidance. *Trends Biotechnol.* 29(5), 213–221 (2011).

134 Shah J, Ma L, Sokolov K *et al.* Photoacoustic imaging and temperature measurement for photothermal cancer therapy. *J. Biomed. Opt.* 13(3), 034024 (2008).

135 Lu W, Melancon MP, Xiong C *et al.* Effects of photoacoustic imaging and photothermal ablation therapy mediated by targeted hollow gold nanospheres in an orthotopic mouse xenograft model of glioma. *Cancer Res.* 71(19), 6116–6121 (2011).

136 Yeager D, Chen Y-S, Litovsky S, Emelianov S. Intravascular photoacoustics for image-guidance and temperature monitoring during plasmonic photothermal therapy of atherosclerotic plaques: a feasibility study. *Theranostics* 4(1), 36–46 (2014).

137 Chang S-S, Shih C-W, Chen C-D, Lai W-C, Wang CC. The shape transition of gold nanorods. *Langmuir* 15(3), 701–709 (1999).

138 Chen Y-S, Frey W, Kim S *et al.* Enhanced thermal stability of silica-coated gold nanorods for photoacoustic imaging and image-guided therapy. *Opt. Express* 18(9), 8867–8878 (2010).

- **Demonstrates that gold nanorods can possess increased photothermal stability and retain their superior optical properties under much higher fluences by coating them with a thin layer of silica.**